

13 **Abstract**

14 Land evapotranspiration (ET) plays a crucial role in Earth's water-carbon cycle, and
15 accurately estimating global land ET is vital for advancing our understanding of land-
16 atmosphere interactions. Despite the development of numerous ET products in recent
17 decades, widely used products still possess inherent uncertainties arising from using
18 different forcing inputs and imperfect model parameterizations. Furthermore, the lack
19 of sufficient global in-situ observations makes direct evaluation of ET products
20 impractical, impeding their utilization and assimilation. Therefore, establishing a
21 reliable global benchmark dataset and exploring evaluation methodologies for ET
22 products is paramount. This study aims to address these challenges by (1) proposing a
23 collocation-based method that considers non-zero error cross-correlation for merging
24 multi-source data and (2) employing this merging method to generate a long-term
25 daily global ET product at resolutions of 0.1° (2000-2020) and 0.25° (1980-2022),
26 incorporating inputs from ERA5L, FluxCom, PMLv2, GLDAS, and GLEAM. The
27 resulting product is the Collocation-Analyzed Multi-source Ensembled Land
28 Evapotranspiration Data (CAMELE). CAMELE exhibits promising performance
29 across various vegetation coverage types, as validated against in-situ observations.
30 The evaluation process yielded Pearson correlation coefficients (R) of 0.63 and 0.65,
31 root-mean-square-errors (RMSE) of 0.81 and 0.73 mm/d, unbiased root-mean-square-
32 errors (ubRMSE) of 1.20 and 1.04 mm/d, mean absolute errors (MAE) of 0.81 and
33 0.73 mm/d, and Kling-Gupta efficiency (KGE) of 0.60 and 0.65 on average over
34 resolutions of 0.1° and 0.25° , respectively. In addition, comparisons indicate that
35 CAMELE can effectively characterize the multi-year linear trend, mean average, and
36 extreme values of ET. However, it exhibits a tendency to overestimate seasonality. In
37 summary, we propose a reliable set of ET data that can aid in understanding the
38 variations in the water cycle and has the potential to serve as a benchmark for various
39 applications.

40 **1. Introduction**

41 Land evapotranspiration (ET) plays a critical role in the global water and energy
42 cycles, encompassing various processes such as soil evaporation, vegetation
43 transpiration, canopy interception, and surface water evaporation (Zhang et al., 2019;
44 Zhao et al., 2022; Lian et al., 2018). Accurately estimating global land
45 evapotranspiration is vital for understanding the hydrological cycle and land-
46 atmosphere interactions, as it serves as an intermediary variable connecting soil
47 moisture, air temperature and humidity (Miralles et al., 2019; Gentile et al., 2019).
48 Therefore, providing a reliable ET dataset as a benchmark for further research is
49 crucial.

50 In recent decades, numerous studies have focused on estimating global land
51 evapotranspiration, resulting in many datasets (Yang et al., 2023). However,
52 discrepancies often arise among these simulations due to algorithm and principle
53 variations (Restrepo-Coupe et al., 2021; Han and Tian, 2020). Additionally,
54 evaluating ET products is challenging due to the limited availability of global-scale
55 observations, which hampers their direct use (Pan et al., 2020; Baker et al., 2021).

56 The fusion of multi-source data is a suitable option to address these uncertainties.
57 Recent studies have explored several approaches to integrate multiple ET products,
58 including Simple Average (SA) (Ershadi et al., 2014), Bayesian Model Average
59 (BMA) (Hao et al., 2019; Ma et al., 2020; Zhu et al., 2016), Reliability Ensemble
60 Average (REA) (Lu et al., 2021), Empirical Orthogonal Functions (EOF) (Feng et al.,
61 2016) and machine-learning-based methods (Chen et al., 2020; Yin et al., 2021).
62 However, the primary challenge lies in calculating reliable input weights based on a
63 selected "truth" (Koster et al., 2021), which can involve averaging or incorporating
64 other relevant geographical information as a benchmark.

65 Recently, collocation methods have emerged as promising techniques for estimating
66 random error variances and data-truth correlations in collocated inputs (Stoffelen,
67 1998; Li et al., 2022, 2023c; Park et al., 2023). These methods consider the errors

68 associated with collocated datasets as an accurate representation of uncertainty
69 without assuming the absence of errors in any datasets. It is important to note that
70 while collocation methods, such as the triple collocation (TC) and the extended
71 double instrumental variable technique (EIVD), can estimate the variance (or
72 covariance) of random errors, they cannot evaluate the bias of the products. One
73 primary advantage of collocation analysis is that it does not require a high-quality
74 reference dataset (Su et al., 2014; Wu et al., 2021). However, a crucial prerequisite for
75 applying collocation methods is the availability of many spatially and temporally
76 corresponding datasets. For instance, the classic TC method requires a trio of
77 independent datasets. Su et al. (2014) used the instrumental regression method and
78 considered lag-1 time series as the third input, proposing the single instrumental
79 variable algorithm (IVS). Dong et al. (2019) introduced the lag-1 time series from
80 both inputs, proposing the double instrumental variable algorithm (IVD) for a more
81 robust solution. Gruber et al. (2016a) extended the original algorithm to incorporate
82 more datasets, partially addressing the independence assumption to calculate a portion
83 of error cross-correlation (ECC) by using the extended collocation (EC) method.
84 Dong et al.(2020a) further proposed the EIVD method, enabling ECC estimation
85 using three datasets. Collocation methods have found widespread application in the
86 evaluation of geophysical variable estimates, including soil moisture (Deng et al.,
87 2023; Ming et al., 2022), precipitation (Dong et al., 2022; Li et al., 2018), ocean wind
88 speed (Vogelzang et al., 2022; Ribal and Young, 2020), leaf area index (Jiang et al.,
89 2017), total water storage (Yin and Park, 2021) sea ice thickness and surface salinity
90 (Hoareau et al., 2018), and near-surface air temperature (Sun et al., 2021).
91 Recently, many studies have utilized collocation approaches to evaluate
92 evapotranspiration products, with the TC method to assess uncertainties. For example,
93 Barraza Bernadas et al. (2018) considered the uncertainties of ET from the Breathing
94 Earth System Simulator, BESS (Jiang et al., 2020; Jiang and Ryu, 2016), Moderate
95 Resolution Imaging Spectroradiometer, MOD16 (Mu et al., 2011), and a hybrid

96 model; Khan et al. (2018) utilized extended triple collocation (ETC) (McColl et al.,
97 2014) to investigate the reliability of ET from MOD16, The Global Land Data
98 Assimilation System (GLDAS) (Rodell et al., 2004) and the Global Land Evaporation
99 Amsterdam Model (GLEAM) (Martens et al., 2017) over East Asia; Li et al. (2022)
100 employed five collocation methods (e.g., IVS, IVD, TC, EIVD, and EC) to analyze
101 the uncertainties of ET from ERA5-Land (ERA5L) (Muñoz-Sabater et al., 2021),
102 GLEAM, GLDAS, FluxCom (Jung et al., 2019), and the Penman-Monteith-Leuning
103 Evapotranspiration V2 (PMLv2) (Zhang et al., 2019).

104 Moreover, error information derived from collocation analysis is valuable for merging
105 multi-source data. This was initially applied by Yilmaz et al. (2012) in the fusion of
106 multi-source soil moisture products and later improved by Gruber et al. (2017) and
107 further applied in the production of the European Space Agency Climate Change
108 Initiative (ESA CCI) global soil moisture product (Gruber et al., 2019). Dong et al.
109 (2020b) also adopted this approach to fusing multi-source precipitation products. In
110 the study of evapotranspiration, Li et al. (2023c) and Park et al.(2023) utilized a
111 weight calculation method that does not consider non-zero ECC and fused multiple
112 ET products in the Nordic and East Asia, respectively, achieving satisfactory fusion
113 results.

114 Although the above studies have demonstrated that collocation analysis can
115 effectively assess the random error variance of ET products and integrate error
116 information from multiple data sources, these studies have primarily overlooked a
117 critical aspect: non-zero ECC between ET products. Li et al. (2022) global ET product
118 evaluation research revealed clear non-zero ECC conditions between ERA5L,
119 GLEAM, PMLv2, and FluxCom. In TC analysis, non-zero ECC can result in
120 significant biases in TC-based results (Yilmaz and Crow, 2014). Furthermore, when
121 using TC-based error information for fusion, it is crucial to consider the information
122 related to ECC, as this can help improve the fusion accuracy (Dong et al., 2020b; Kim
123 et al., 2021b).

124 It is worth noting that non-zero ECC conditions pose unique challenges. Unlike other
125 violations of mathematical assumptions adopted by TC, they cannot be effectively
126 mitigated through rescaling or compensated for by equal magnitude adjustments
127 across inputs. Thus, the implications of non-zero ECC in the context of merging
128 strategies are a critical consideration often overlooked in previous research. This
129 oversight can lead to significant biases and inaccuracies. We aim to bridge this gap by
130 systematically accounting for non-zero ECC in weight calculation, contributing to a
131 more robust and accurate assessment.

132 In this study, we proposed a collocation-based data ensemble method, considering
133 non-zero ECC conditions, for merging multiple ET products to create the Collocation-
134 Analyzed Multi-source Ensembled Land Evapotranspiration data, abbreviated as
135 CAMELE. The second section of this paper presents the selected data information for
136 this study. In the third section, we explained the error calculation method for
137 collocation analysis and the weighted calculation method that considered ECC. The
138 fourth section analyzed the global errors of different ET products obtained through
139 these calculations and the distribution patterns of the corresponding weights. We
140 evaluated the accuracy of the fused products and compared them with existing
141 products using reference values from site measurements. In the fifth section, we
142 discussed the inherent errors in the methods, analyzed the ECC between the products,
143 and compared the differences between different fusion schemes. Finally, in the sixth
144 section, we summarized the results obtained from this research.

145 **2. Datasets**

146 We selected five widely used ET products that spanned the period from 1980 to 2022.
147 When selecting these products, our aims are to ensure: (1) consistency in original
148 spatiotemporal resolution among the products: minimize potential downscaling
149 operations and avoid introducing additional errors; (2) having three or more products
150 within the same resolution or period: incorporate more information for effective

151 fusion; (3) products with extensive global observational sequences: gain basic
 152 recognition from the community. While we acknowledge the existence of other
 153 higher-precision products, their integration would require either downscaling or
 154 upscaling other products, potentially introducing uncertainties. Therefore, we chose
 155 the combination outlined in the manuscript. Despite its relatively lower resolution
 156 compared to some products, it still contributes to our understanding of ET variations,
 157 facilitating advantageous exploration. Furthermore, we incorporated in-situ
 158 observations and Lu et al.'s (2021) global 0.25° daily-scale ET product derived using
 159 Reliability Ensemble Averaging (denoted as REA) to compare our merged product
 160 comprehensively. **Table 1** shows the spatial and temporal resolutions of the input
 161 datasets.

162 **Table 1** Summary of evapotranspiration products involved.

Name	Schemes	Resolution	Period	Reference	
ERA5-Land	H-TESSSEL	0.1°	hourly	1950-present	(Muñoz-Sabater et al., 2021)
GLDAS-2	CLSM/Noah /LSM	0.25°	3-hourly daily	2.0: 1948-2014 2.1: 2000-present 2.2: 2003-present	(Li et al., 2019a; Rodell et al., 2004)
GLEAM-3.7	GLEAM model	0.25°	daily	3.7a: 1980-2022 3.7b: 2003-2022	(Martens et al., 2017)
PMLv2-v017	Penman- Monteith- Leuning	0.083°	8-day average	2000-2020	(Zhang et al., 2019)
FluxCom	Machine learning	0.083°	8-day average	2001-2015	(Jung et al., 2019)

163 **2.1. ERA5-Land**

164 The European Centre for Medium-Range Weather Forecasts (ECMWF) produces the
 165 latest advanced ERA5L, a global hourly reanalysis dataset with a spatial resolution of

166 0.1°. It covers the period from January 1950 until approximately one week before the
167 present (Muñoz-Sabater et al., 2021). ERA5-Land is derived from the land component
168 of the ECMWF climate reanalysis, incorporating numerous improvements over
169 previously released versions. It is based on the Tiled ECMWF Scheme for Surface
170 Exchanges over Land incorporating land surface hydrology (H-TESSSEL), utilizing
171 version CY45R1 of the ECMWF's Integrated Forecasting System (IFS). The dataset
172 benefits from atmospheric forcing data, which acts as an indirect constraint on the
173 model-based estimates (Hersbach et al., 2020). The dataset is available through the
174 Climate Change service of the Copernicus Center at <http://cds.climate.copernicus.eu>.
175 Evapotranspiration in ERA5L, defined as "total evaporation," represents the
176 accumulated amount of water that has evaporated from the Earth's surface, including a
177 simplified representation of transpiration from vegetation into the vapor in the air.
178 The soil water and energy balance are computed using standard soil discretization.
179 Readers could consult section 8.6.5 of the IFS documentation (ECMWF, 2014). The
180 original dataset is interpolated from (1801, 3600) to (1800, 3600) using kriging
181 interpolation and then upscaled from an hourly to a daily resolution, changing spatial
182 resolution from 0.1° to 0.25°.

183 **2.2. GLDAS**

184 The Global Land Data Assimilation System (GLDAS) product utilizes advanced data
185 assimilation methodologies, integrating model and observation datasets for land-
186 surface simulations (Rodell et al., 2004). GLDAS employs multiple land-surface
187 models (LSMs), namely Noah, Mosaic, Variable Infiltration Capacity (VIC), and the
188 Community Land Model (CLM). Together, these models generate global
189 evapotranspiration estimates at fine and coarse spatial resolutions (0.01° and 0.25°)
190 and temporal resolutions (3-hourly and monthly). The most recent iteration of
191 GLDAS, version 2, consists of three components: GLDAS-2.0, GLDAS-2.1, and
192 GLDAS-2.2. GLDAS-2.0 relies entirely on the Princeton meteorological forcing input

193 data, providing a consistent temporal series from 1948 to 2014 (Sheffield et al., 2006).
194 The GLDAS-2.1 simulation commences on January 1, 2000, utilizing the conditions
195 from the GLDAS-2.0 simulation. On the other hand, GLDAS-2.2 is simulated from
196 February 1, 2003, employing the conditions from GLDAS-2.0 and forcing with
197 meteorological analysis fields from the ECMWF Integrated Forecasting System (IFS).
198 Additionally, the GRACE satellite's total terrestrial water anomaly observation is
199 assimilated into the GLDAS-2.2 product (Li et al., 2019a).

200 This study aimed to cover the research period from 1980 to 2022. Non-zero ECC
201 between the transpiration estimates of GLDAS-2.2 and ERA5L has been reported in a
202 recent study (Li et al., 2023a). Considering the similarities in the calculation of ET
203 and transpiration of GLDAS and ERA5L, this report partially indicates a correlation.
204 Therefore, GLDAS-2.0 and GLDAS-2.1 were selected as inputs instead. The
205 "Evap_tavg" parameter representing evapotranspiration is derived from the original
206 products and aggregated to a daily scale. For more detailed information on the
207 GLDAS-2 models, please refer to NASA's Hydrology Data and Information Services
208 Center at <http://disc.sci.gsfc.nasa.gov/hydrology>.

209 Despite the same forcing between GLDAS-2.1 and GLDAS-2.2, significant
210 differences exist between the model results of different GLDAS versions (Qi et al.,
211 2020, 2018; Jiménez et al., 2011). The non-zero ECC will generally still be met
212 between different versions. Thus, we still need to analyze the non-zero ECC situations
213 between ERA5L and GLDAS-2.0 and 2.1, which will be assessed in the discussion
214 sections.

215 **2.3. GLEAM**

216 The version of the Global Land Evaporation Amsterdam Model 3.7 (GLEAM-3.7)
217 dataset (Martens et al., 2017; Miralles et al., 2011) at 0.25° is used. This version of
218 GLEAM provides daily estimations of actual evaporation, bare soil evaporation,
219 canopy interception, transpiration from vegetation, potential evaporation, and snow

220 sublimation. The third version of GLEAM contains a new DA scheme, an updated
221 water balance module, and evaporative stress functions. Two datasets that differ only
222 in forcing and temporal coverage are provided: GLEAMv3.7a-43-year period (1980
223 to 2022) based on satellite and reanalysis (ECMWF) data; GLEAMv3.7b-20-year
224 period (2003 to 2022) based on only satellite data. GLEAMv3.7a is used in this study.
225 The data are freely available on the GLEAM website (<https://www.gleam.eu>).
226 The cover-dependent potential evaporation rate (E_p) is calculated using the Priestley-
227 Taylor equation (Priestley and TAYLOR, 1972). Then a multiplicative stress factor is
228 used to convert E_p into actual transpiration and bare soil evaporation, which is the
229 function of microwave vegetation optimal depth (VOD) and root-zone soil moisture.
230 For detailed description, please refer to the paper by Martens et al., (2017). The
231 GLEAM data were validated at 43 FluxNet flux sites and have been proven to provide
232 reliable ET estimations (Majozi et al., 2017).

233 **2.4. PMLv2**

234 The Penman-Monteith-Leuning version 2 global evaporation model (PMLv2) has
235 been developed based on the Penman-Monteith-Leuning model (Zhang et al., 2019;
236 Leuning et al., 2009). Initially proposed by Leuning et al. (2008), the PML model
237 underwent further enhancements by Zhang et al. (2010). The PML version 1 (PMLv1)
238 incorporates a biophysical model that considers canopy physiological processes and
239 soil evaporation to estimate surface conductance accurately (G_s), which is the focus of
240 the PM-based method. This version was subsequently enhanced by incorporating a
241 canopy conductance (G_c) model that couples vegetation transpiration with gross
242 primary productivity, resulting in the development of PML version 2 (PMLv2) as
243 described by Gan et al. (2018). Zhang et al. (2019) applied the PMLv2 model globally.
244 The daily inputs for this model include leaf area index (LAI), broadband albedo, and
245 emissivity obtained from the Moderate Resolution Imaging Spectroradiometer
246 (MODIS), as well as temperature variables (daily maximum temperature- T_{max} , daily

247 minimum temperature- T_{min} , daily mean temperature- T_{avg}), instantaneous variables
248 (surface pressure- P_{surf} , atmosphere pressure- P_a , wind speed at 10-meter height- U ,
249 specific humidity- q), and accumulated variables (precipitation- P_{rcp} , inward longwave
250 solar radiation- R_{ln} , inward shortwave solar radiation- R_s) from GLDAS-2.0.
251 Evaporation is divided into direct evaporation from bare soil (E_s), evaporation from
252 solid water sources (water bodies, snow, and ice) (ET_{water}), and vegetation
253 transpiration (E_c). To ensure its accuracy, the PMLv2-ET model was calibrated
254 against 8-daily eddy covariance data from 95 global flux towers representing ten
255 different land cover types.

256 In this study, we employ the latest version, v017. The data is freely available through
257 the google earth engine [https://developers.google.com/earth-](https://developers.google.com/earth-engine/datasets/catalog/CAS_IGSNRR_PML_V2_v017)
258 [engine/datasets/catalog/CAS_IGSNRR_PML_V2_v017](https://developers.google.com/earth-engine/datasets/catalog/CAS_IGSNRR_PML_V2_v017).

259 **2.5. FluxCom**

260 FluxCom is a machine-learning-based approach combining global land-atmosphere
261 energy flux data by combining remote sensing and meteorological data (Jung et al.,
262 2019). To achieve this, FluxCom utilizes various machine-learning regression tools,
263 including tree-based methods, regression splines, neural networks, and kernel
264 methods. The outputs of FluxCom are designed based on two complementary
265 strategies: (1) FluxCom-RS, which exclusively merges remote sensing data to
266 generate high spatial resolution flux data; and (2) FluxCom-RS+METEO, which
267 combines meteorological observations with remote sensing data at a daily temporal
268 resolution. The exclusive use of remote sensing data in the ensemble allows
269 producing gridded flux products at a spatial resolution of 500m, albeit with a
270 relatively low frequency of 8 days. It is important to note that the FluxCom-RS data
271 only covers the period after 2000 due to data availability.

272 In contrast, the merging of meteorological and remote sensing data extends the
273 coverage back to 1980 at the cost of a coarser spatial resolution of 0.5° . For more

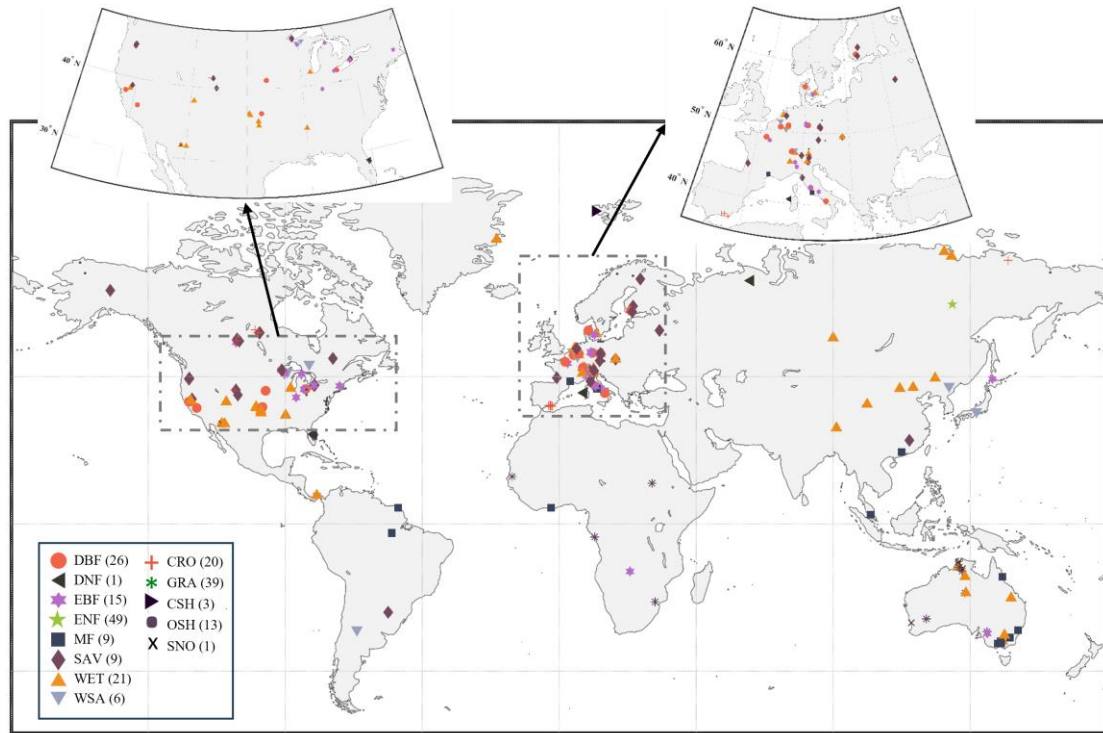
274 detailed information about the FluxCom dataset, please refer to the FluxCom website
275 (<http://FluxCom.org/>). The data is freely available upon contacting the authors.
276 In this study, we utilized the FluxCom-RS 8-daily 0.0833° energy flux data and
277 converted the latent heat values to evapotranspiration using ERA5L aggregated daily
278 air temperature. Furthermore, the original ET data were interpolated to a spatial
279 resolution of 0.1° using the MATLAB Gaussian process regression package.

280 **2.6. Global in-situ observation: FluxNet**

281 The latest FluxNet2015 4.0 eddy-covariance data were used in our study (Pastorello et
282 al., 2020). Following the filtering process by Lin et al. (2018) and Li et al. (2019b),
283 firstly, only the measured and good-quality gap-filled data were used for quality
284 control. Secondly, we excluded days with rainfall and the subsequent day after rainy
285 events to mitigate the impact of canopy interception (Medlyn et al., 2017; Knauer et
286 al., 2018). Additionally, previous studies have indicated an energy imbalance problem
287 in FluxNet2015 data. Therefore, following the method proposed by Twine et al.
288 (2000), the measured ET data were corrected using the residual method based on
289 energy balance.

290 After data filtering and processing, 212 sites are selected as shown in **Figure 1**. The
291 selected sites are distributed globally, primarily in North America and Europe. The
292 International-Geosphere–Biosphere Program (IGBP) land cover classification system
293 (Loveland et al., 1999) was employed to distinguish the 13 Plant Functional Types
294 (PFTs) across sites. The IGBP classification was determined based on metadata from
295 the FluxNet official website, including evergreen needle leaf forests (ENF, 49 sites),
296 evergreen broadleaf forests (EBF, 15 sites), deciduous broadleaf forests (DBF, 26
297 sites), croplands (CRO, 20 sites), grasslands (GRA, 39 sites), savannas (SAV, 9 sites),
298 mixed forests (MF, 9 sites), closed shrublands (CSH, 3 sites), deciduous needle leaf
299 forests (DNF, 1 site), open shrublands (OSH, 13 sites), snow and ice (SNO, 1 site),
300 woody savannas (WSA, 6 sites) and permanent wetland (WET, 21 sites). Changes in

301 the IGBP classification during the study period are possible, but such information is
302 not publicly available. Interested parties can obtain relevant information by directly
303 contacting the site coordinators.



304

305

Figure 1 Global distribution of selected FluxNet Sites.

306 **3. Method**

307 In this study, the fusion of products consisted of three steps: (1) the collocation
308 method (IVD and EIVD) was used to calculate the random error variance of the
309 selected input products, determine the regionally optimal products, and set an error
310 threshold; (2) aiming for minimum mean-square-error (MSE), the weights of different
311 products on each grid were calculated; (3) the products were fused according to the
312 weights to obtain a long sequence of evapotranspiration products. Since IVD and
313 EIVD were developed by combining instrumental variable regression and the
314 extended collocation system, a description of TC and EC algorithms was also
315 included.

316 3.1. Triple collocation analysis

317 Since its development in 1998, the implications and formulations of the triple
318 collocation problem have been investigated in many studies. Here, we used difference
319 notation for demonstration.

320 The commonly used error structure for triple collocation analysis (TCA) is:

$$i = \alpha_i + \beta_i \Theta + \varepsilon_i \quad (1)$$

321 where $i \in [X, Y, Z]$ are three spatially and temporally collocated data sets; Θ is the
322 unknown true signal for relative geographical variable; α_i and β_i are additive and
323 multiplicative bias factors against the true signal, respectively; ε_i is the additive zero-
324 mean random error.

325 The above structure is also a typical instrumental variable (IV) regression. Thus, this
326 provides another perspective to introduce more variables (>3) (Dong and Crow, 2017;
327 Su et al., 2014) and polynomial models (Yilmaz and Crow, 2013; De Lannoy et al.,
328 2007) to the standard TC. We recommend that the readers refer to Su et al. (2014) for
329 a more detailed discussion on using the IV framework.

330 The basic assumptions adopted in TC are as follows: (i) Linearity between true signal
331 and data sets, (ii) signal and error stationarity, (iii) independency between random
332 error and true signal (error orthogonality), (iv) independence between random errors
333 (zero ECC). Although many studies have indicated that some of these assumptions are
334 often violated in practice (Li et al., 2018, 2022; Jia et al., 2022), the formulation based
335 on these assumptions is still the most robust implementation (Gruber et al., 2016b). A
336 discussion on these assumptions will be provided in the discussion section.

337 The data sets first need to be rescaled against an arbitrary reference (e.g., X). The
338 others are scaled through a TC-based rescaling scheme:

$$Y^X = \beta_Y^X (Y - \bar{Y}) + \bar{X} \quad Z^X = \beta_Z^X (Z - \bar{Z}) + \bar{X} \quad (2)$$

339 The overbar denotes the mean value, and β_Y^X and β_Z^X are the scaling factors as:

$$\begin{cases} \beta_Y^X = \frac{\beta_X}{\beta_Y} = \frac{\langle (X - \bar{X})(Z - \bar{Z}) \rangle}{\langle (Y - \bar{Y})(Z - \bar{Z}) \rangle} = \frac{\sigma_{XZ}}{\sigma_{YZ}} \\ \beta_Z^X = \frac{\beta_X}{\beta_Z} = \frac{\langle (X - \bar{X})(Y - \bar{Y}) \rangle}{\langle (Z - \bar{Z})(Y - \bar{Y}) \rangle} = \frac{\sigma_{XY}}{\sigma_{ZY}} \end{cases} \quad (3)$$

340 where $\langle \cdot \rangle$ is the average operator, σ_{ij} is the covariance of data sets i and j .

341 Subsequently, the error variances could be estimated by averaging the cross-
342 multiplied data set differences as follows:

$$\begin{cases} \sigma_{\varepsilon_X}^2 = \langle (X - Y^X)(X - Z^X) \rangle \\ \sigma_{\varepsilon_Y}^2 = \beta_Y^{X^2} \sigma_{\varepsilon_Y}^2 = \langle (Y^X - X)(Y^X - Z^X) \rangle \\ \sigma_{\varepsilon_Z}^2 = \beta_Z^{X^2} \sigma_{\varepsilon_Z}^2 = \langle (Z^X - X)(Z^Y - Y^X) \rangle \end{cases} \quad (4)$$

343 Expanding the bracket and expressing the rescaling factors yields:

$$\begin{cases} \sigma_{\varepsilon_X}^2 = \sigma_X^2 - \frac{\sigma_{XY}\sigma_{XZ}}{\sigma_{YZ}} \\ \sigma_{\varepsilon_Y}^2 = \sigma_Y^2 - \frac{\sigma_{YX}\sigma_{YZ}}{\sigma_{XZ}} \\ \sigma_{\varepsilon_Z}^2 = \sigma_Z^2 - \frac{\sigma_{ZX}\sigma_{ZY}}{\sigma_{XY}} \end{cases} \quad (5)$$

344 When selecting various scaling references, it is essential to note that the absolute error
345 variances remain consistent. However, this choice can have an impact on the
346 estimation of data sensitivity to the actual signal ($\beta_i^2 \sigma_{\Theta}^2$), which serves as a crucial
347 indicator for comparing spatial error patterns. In order to address the reliance on a
348 specific scaling reference, Draper et al. (2013) introduced the fractional root-mean-
349 squared-error ($fMSE_i$). This measure is obtained by normalizing the unscaled error
350 variance with respect to the true signal variance:

$$fMSE_i = \frac{\sigma_{\varepsilon_i}^2}{\sigma_i^2} = \frac{\sigma_{\varepsilon_i}^2}{\beta_i^2 \sigma_{\Theta}^2 + \sigma_{\varepsilon_i}^2} = \frac{1}{1 + SNR_i} \quad (6)$$

351 where $SNR_i = \frac{\beta_i^2 \sigma_{\Theta}^2}{\sigma_{\varepsilon_i}^2} \in [0,1]$ is the normalized signal-to-noise ratio. $SNR = 0$
352 indicates a noise-free observation, while $SNR = 1$ corresponds that the variances of
353 estimates equal that of the true signal.

354 Following similar ideas, Mccoll et al. (2014) extended the framework to estimate the

355 data-truth correlation, known as the ETC:

$$R_i^2 = \frac{\beta_i^2 \sigma_\Theta^2}{\beta_i^2 \sigma_\Theta^2 + \sigma_{\varepsilon_i}^2} = \frac{SNR_i}{1 + SNR_i} \quad (7)$$

$$R_i^2 = 1 - fMSE_i$$

356 In comparison to the conventional coefficient of determination R_{ij} , which is
 357 influenced by data noise and sensitivity. It is important to note that R_i^2 is merely based
 358 on the data set i , whereas R_{ij} is influenced by both data set i and reference j . In other
 359 words, R_i^2 incorporates the dependency on the chosen reference. Thus, TC-derived
 360 $fMSE_i$ and R_i^2 serve as superior indicators for assessing the actual quality of data, as
 361 discussed by Kim et al. (2021b) and Gruber et al. (2020).

362 3.2. Double instrumental variable technique

363 The assumed error structure in TC is also a typical instrumental variable (IV)
 364 regression. In practical usage, finding three completely independent sets of products is
 365 usually tricky. Su et al. (2014) effectively improve the applicability of the TC method
 366 by using the lag-1 time series (e.g., $X_{t-1} = \alpha_X + \beta_X \Theta_{t-1} + \varepsilon_{X,t-1}$) from one of the
 367 two sets of data as the third input for TC. In this way, we only need two independent
 368 products for input.

369 Such process includes another assumption that all data sets contain serially white
 370 errors (i.e., $\langle \varepsilon_{i,t} \varepsilon_{i,t-1} \rangle = 0$, zero auto-correlation). Building upon this, Dong et al.
 371 (2019) utilizes the lag-1 time series from both data sets as inputs and propose the
 372 more stable IVD method.

373 For a double input $[X, Y$ with $\sigma_{\varepsilon_X \varepsilon_Y} = 0]$, the linear error model and related lag-1
 374 time series can be expressed as:

$$\begin{cases} X = \alpha_X + \beta_X \Theta + \varepsilon_X & I = \alpha_X + \beta_X \Theta_{t-1} + \varepsilon_{X,t-1} \\ Y = \alpha_Y + \beta_Y \Theta + \varepsilon_Y & J = \alpha_Y + \beta_Y \Theta_{t-1} + \varepsilon_{Y,t-1} \end{cases} \quad (8)$$

375 where I and J are the lag-1 time series of X and Y , respectively.

376 Assuming product errors are mutually independent and orthogonal to the truth, the

377 covariance between the products is expressed as:

$$\begin{cases} \sigma_X^2 = \beta_X^2 \sigma_\Theta^2 + \sigma_{\varepsilon_X}^2 & \sigma_Y^2 = \beta_Y^2 \sigma_\Theta^2 + \sigma_{\varepsilon_Y}^2 \\ \sigma_{XY} = \beta_X \beta_Y \sigma_\Theta^2 \\ \sigma_{IX} = \beta_X^2 L_{\Theta\Theta} & \sigma_{JY} = \beta_Y^2 L_{\Theta\Theta} \end{cases} \quad (9)$$

378 where $L_{ii} = \langle i_t i_{t-1} \rangle$ is the auto-covariance. Therefore, the IVD-estimated dynamic
379 range ratio scaling factors yields:

$$s_{ivd} \equiv \frac{\beta_X}{\beta_Y} = \sqrt{\frac{\sigma_{IX}}{\sigma_{JY}}} \quad (10)$$

380 Hence, the random error variances of X and Y can be solved as:

$$\begin{cases} \sigma_{\varepsilon_X}^2 = \sigma_X^2 - \sigma_{XY} * s_{ivd} \\ \sigma_{\varepsilon_Y}^2 = \sigma_Y^2 - \frac{\sigma_{XY}}{s_{ivd}} \end{cases} \quad (11)$$

381 3.3. Extended double instrumental variable technique

382 Furthermore, by adopting the designed matrix in the EC method (Gruber et al., 2016a),
383 Dong et al. (2020a) present the EIVD method to estimate the error variance matrix
384 with only two independent data sets.

385 For a triplet input $[i, j, k$ with $\sigma_{\varepsilon_i \varepsilon_j} \neq 0]$. The dynamic range ratio scaling factors can
386 be estimated as follows:

$$s_{ij} \equiv \frac{\beta_i}{\beta_j} = \sqrt{\frac{L_{ii}}{L_{jj}}} \quad (12)$$

387 where $L_{ii} = \langle i_t i_{t-1} \rangle$ is the auto-covariance of inputs. Subsequently, the sensitivity
388 and absolute error variance of the data set follow:

$$\beta_j^2 \sigma_\Theta^2 = \sigma_{ij} \sqrt{\frac{L_{ii}}{L_{jj}}} \quad \sigma_{\varepsilon_j}^2 = \sigma_{ij} \sqrt{\frac{L_{ii}}{L_{jj}}} - \sigma_i^2 \quad (13)$$

389 The cross-multiplied factors can be estimated by:

$$\beta_i \beta_j \sigma_\Theta^2 = \sigma_{ik} \sqrt{\frac{L_{jj}}{L_{kk}}} = \sigma_{jk} \sqrt{\frac{L_{ii}}{L_{kk}}} \quad \sigma_{\varepsilon_i \varepsilon_j} = \sigma_{ij} - \beta_i \beta_j \sigma_\Theta^2 \quad (14)$$

390 Hence, for a triplet with the input of $[X, Y, Z$ with $\sigma_{\varepsilon_X \varepsilon_Y} \neq 0]$: the matrix notation of
 391 the above system with $\mathbf{y} = \mathbf{A}\mathbf{x}$ is given as:

$$\mathbf{y} = \begin{pmatrix} \sigma_X^2 \\ \sigma_Y^2 \\ \sigma_Z^2 \\ \sigma_{XY} \\ \sigma_{XZ} \sqrt{\frac{L_{XX}}{L_{ZZ}}} \\ \sigma_{YZ} \sqrt{\frac{L_{YY}}{L_{ZZ}}} \\ \sigma_{ZX} \sqrt{\frac{L_{ZZ}}{L_{XX}}} \\ \sigma_{ZY} \sqrt{\frac{L_{ZZ}}{L_{YY}}} \\ \sigma_{XZ} \sqrt{\frac{L_{YY}}{L_{ZZ}}} \\ \sigma_{YZ} \sqrt{\frac{L_{XX}}{L_{ZZ}}} \end{pmatrix}_{10 \times 1} \quad \mathbf{A} = \begin{pmatrix} \mathbf{I}_{4 \times 4} & \mathbf{I}_{4 \times 4} \\ \mathbf{0}_{6 \times 4} & \mathbf{0}_{6 \times 4} \end{pmatrix}_{10 \times 8} \quad \mathbf{x} = \begin{pmatrix} \beta_X^2 \sigma_\theta^2 \\ \beta_Y^2 \sigma_\theta^2 \\ \beta_Z^2 \sigma_\theta^2 \\ \beta_X \beta_Y \sigma_\theta^2 \\ \sigma_{\varepsilon_X}^2 \\ \sigma_{\varepsilon_Y}^2 \\ \sigma_{\varepsilon_Z}^2 \\ \sigma_{\varepsilon_X \varepsilon_Y} \end{pmatrix}_{8 \times 1} \quad (15)$$

392 Likewise, the least-squared solution for unknown \mathbf{x} is then solved by:

$$\mathbf{x} = (\mathbf{A}^T \mathbf{A})^{-1} \mathbf{A}^T \mathbf{y} \quad (16)$$

393 3.4. Weight Estimation

394 Our objective is to predict an uncertain variable, such as evapotranspiration (ET) over
 395 time at a specific location, by utilizing parent products that may contain random errors.
 396 The underlying concept of weighted averaging is to extract independent information
 397 from multiple data sources to enhance prediction accuracy by mitigating the effects of
 398 random errors. The effectiveness of this approach relies on the independence of the
 399 individual data sources under consideration. Weighted averaging has found
 400 applications in various fields following the influential work of Bates and Granger
 401 (1969), who proposed the optimal combination of forecasts based on a minimum
 402 MSE criterion. In this context, the term "optimal" refers to minimizing the variance of
 403 residual random errors in the least squares sense. Mathematically, this weighted

404 average can be expressed as follows:

$$\bar{x} = \bar{\mathbf{W}}^T \bar{\mathbf{X}} = \sum_{i=1}^N \omega_i x_i \quad (17)$$

405 where \bar{x} is the merged estimate; $\bar{\mathbf{X}} = [x_1, \dots, x_n]^T$ contains the temporally collocated
 406 estimates from N different parent products, which are merged with relative zero-mean
 407 random error $\bar{\mathbf{e}} = [\varepsilon_1, \dots, \varepsilon_n]^T$; and $\bar{\mathbf{W}} = [\omega_1, \dots, \omega_n]^T$ contains the weights assigned
 408 to these estimates, where $\omega_i \in [0,1]$ and $\sum \omega_i = 1$ ensuring an unbiased prediction.

409 The averaging weights can be expressed as the solution to the problem:

$$\min f(\bar{\mathbf{W}}) = \mathbb{E}(\bar{\mathbf{e}}^T \bar{\mathbf{W}})^2 \quad (18)$$

410 where $\mathbb{E}()$ is the operator for mathematical expectation, the solution of this problem is
 411 determined by the individual random error characteristics of the input data sets and
 412 can be derived from their covariance matrix (Bates and Granger, 1969; Gruber et al.,
 413 2017; Kim et al., 2021b):

$$\begin{aligned} \bar{\mathbf{W}} &= (\bar{\mathbf{I}}^T \mathbb{E}(\bar{\mathbf{e}}\bar{\mathbf{e}}^T) \bar{\mathbf{I}})^{-1} \mathbb{E}(\bar{\mathbf{e}}\bar{\mathbf{e}}^T) \bar{\mathbf{I}} \\ \sigma_{\bar{x}}^2 &= (\bar{\mathbf{I}}^T \mathbb{E}(\bar{\mathbf{e}}\bar{\mathbf{e}}^T) \bar{\mathbf{I}})^{-1} \end{aligned} \quad (19)$$

414 where $\mathbb{E}(\bar{\mathbf{e}}\bar{\mathbf{e}}^T)$ is the $N \times N$ error covariance matrix that holds the random error
 415 variance $\sigma_{\varepsilon_i}^2$ of the parent products in the diagonals and relative error covariances $\sigma_{\varepsilon_i \varepsilon_j}$
 416 in the off-diagonals; $\bar{\mathbf{I}} = [1, \dots, 1]^T$ is an ones-vector of length N ; and $\sigma_{\bar{x}}^2$ is the
 417 resulting random error variances of the merged estimate.

418 When only two groups of products are used as input ($N = 2$), it is generally assumed
 419 that the errors between them are independent. In this case, the weights are as follows:

$$\begin{aligned} \mathbb{E}(\bar{\mathbf{e}}\bar{\mathbf{e}}^T) &= \begin{bmatrix} \sigma_{\varepsilon_1}^2 & 0 \\ 0 & \sigma_{\varepsilon_2}^2 \end{bmatrix} \\ \omega_1 &= \frac{\sigma_{\varepsilon_2}^2}{\sigma_{\varepsilon_1}^2 + \sigma_{\varepsilon_2}^2} \quad \omega_2 = \frac{\sigma_{\varepsilon_1}^2}{\sigma_{\varepsilon_1}^2 + \sigma_{\varepsilon_2}^2} \end{aligned} \quad (20)$$

420 In most cases, we can identify three sets of products as inputs ($N = 3$). In this
 421 scenario, we consider the possibility of error homogeneity, assuming a non-zero ECC

422 exists between inputs 1 and 2. In this case, the error matrix can be represented as:

$$\mathbb{E}(\vec{e}\vec{e}^T) = \begin{bmatrix} \sigma_{\varepsilon_1}^2 & \sigma_{\varepsilon_1\varepsilon_2} & 0 \\ \sigma_{\varepsilon_1\varepsilon_2} & \sigma_{\varepsilon_2}^2 & 0 \\ 0 & 0 & \sigma_{\varepsilon_3}^2 \end{bmatrix} \quad (21)$$

423 The weights can then be written as:

$$\vec{W} = \begin{cases} \frac{\sigma_{\varepsilon_2}^2 - \sigma_{\varepsilon_1\varepsilon_2}}{(\sigma_{\varepsilon_1}^2 \sigma_{\varepsilon_2}^2 - \sigma_{\varepsilon_1\varepsilon_2}^2) * \mathbb{Z}} \\ \frac{\sigma_{\varepsilon_1}^2 - \sigma_{\varepsilon_1\varepsilon_2}}{(\sigma_{\varepsilon_1}^2 \sigma_{\varepsilon_2}^2 - \sigma_{\varepsilon_1\varepsilon_2}^2) * \mathbb{Z}} \\ \frac{1}{\sigma_{\varepsilon_3}^2 * \mathbb{Z}} \end{cases} \quad (22)$$

$$\mathbb{Z} = \frac{\sigma_{\varepsilon_1}^2 + \sigma_{\varepsilon_2}^2 - 2\sigma_{\varepsilon_1\varepsilon_2}}{\sigma_{\varepsilon_1}^2 \sigma_{\varepsilon_2}^2 - \sigma_{\varepsilon_1\varepsilon_2}^2} + \frac{1}{\sigma_{\varepsilon_3}^2}$$

424 It is essential to acknowledge that before applying these weights for merging the data
 425 sets, it is necessary to address any existing systematic differences. Typically, this is
 426 achieved by rescaling the data sets to a standardized data space. Consequently, the
 427 weights can be derived from the rescaled data sets using Eq (2)-(3) and converge
 428 accordingly. This procedure ensures the accuracy and reliability of the merged data
 429 sets for further analysis.

430 If ECC is not considered (i.e., setting $\sigma_{\varepsilon_1\varepsilon_2} = 0$), Eq (22) represents the weight
 431 calculation method commonly used in most TC fusion studies. In contrast to the
 432 fusion studies mentioned above for evapotranspiration products, for the first time, the
 433 consideration of non-zero ECC is incorporated into the fusion process and integrated
 434 into the weight calculation. Yilmaz and Crow (2014) have demonstrated that TC
 435 underestimates error variances when the zero ECC assumption is violated. Li et al.
 436 (2022), in their evaluation study of global ET products using the collocation method,
 437 also indicated the existence of error homogeneity issues between commonly used ET
 438 products (such as ERA5L and GLEAM), necessitating the consideration of the
 439 influence of non-zero ECC. The merging technique employed in this study provides a
 440 more explicit characterization of product errors and facilitates the derivation of more

441 reliable weight coefficients, thereby achieving promising fusion outcomes.
442 The differences in results are evaluated at the site scale by contrasting the scenarios
443 without considering non-zero ECC and directly using simple averages to compare and
444 validate the advantages of the weight calculation method used in our study.

445 **3.5. Merging combination**

446 In this study, we employ five commonly used global land surface ET products as
447 described in the datasets section. PMLv2 and FluxCom-RS have an original resolution
448 of 0.083° and an 8-day average. In this research, they are interpolated to 0.1°
449 resolution, and the values for each data period of 8 days are kept consistent. For
450 example, the values for March 5 to March 12, 2000, are the same. ET values often
451 exhibit variability over an 8-day period, making the use of an 8-day average to
452 represent temporal dynamics potentially introducing further uncertainties. This
453 operation is performed to ensure adequate data for the collocation analysis (Kim et al.,
454 2021a). We openly acknowledge the possible sources of error and express our
455 commitment to addressing and improving them in future work.

456 As mentioned in the methodology section, it is vital to consider the issue of random
457 error homogeneity among different products before applying the collocation method.
458 Although EC or EIVD methods can be used to calculate the ECC between specific
459 pairs of products, it is necessary to determine which pairs of products have non-zero
460 ECC conditions. In previous research, Li et al.(2022) employed five collocation
461 methods (IVS/IVD/TC/EIVD/EC) to analyze the performance of five sets of ET
462 products (ERA5L/ PMLv2/FluxCom/GLDAS2/GLEAMv3) at the global scale, and
463 applied EC and EIVD methods to calculate the ECC between different products. The
464 results indicated a relatively significant error homogeneity between PMLv2 and
465 FluxCom at a resolution of 0.1° (with a global average ECC of approximately 0.3).
466 The error homogeneity could be attributed to both products utilizing GLDAS
467 meteorological data as input, despite their different methods for ET estimation. At a

468 resolution of 0.25° , ERA5L and GLEAM exhibited a more apparent error correlation
 469 (with a global average ECC of approximately 0.4). Considering the long temporal
 470 data of GLEAMv3 version a, ECMWF meteorological data was chosen as the driving
 471 force, making the error correlation between the two products predictable.

472 Therefore, this study assumes that non-zero ECC situations occur between PMLv2-
 473 FluxCom and ERA5L-GLEAM. We also calculated the possible ECC situations
 474 among other products, presented in the discussion section and the appendix. Based on
 475 the analysis, our assumed non-zero ECC situations align reasonably well with the
 476 actual circumstances.

477 In addition, previous research suggests that the IVD method outperforms the IVS
 478 method in scenarios involving two sets of inputs, while the EIVD method is
 479 considered more reliable than the TC method in situations with three sets of inputs (Li
 480 et al., 2022; Kim et al., 2021a). Therefore, in this study, the IVD and EIVD methods
 481 are selected for computation based on different combinations of inputs. **Table 2**
 482 presents the data and methods used during corresponding periods. When only two sets
 483 of products are available, we employ the IVD method for fusion and calculate weights
 484 using Eq. (20). When three sets of products are available, we utilize the EIVD method
 485 for fusion and calculate weights using Eq. (22).

486 **Table 2** Combination of inputs and accessible methods

Scenario 1 (0.1°)		
Period	Selected Inputs	Method
(2000.02.26-2000.12.31)	ERA5L/ PMLv2	IVD
(2001.01.01-2015.12.27)	ERA5L/ FluxCom/ PMLv2	EIVD
(2015.12.28-2020.12.26)	ERA5L/ PMLv2	IVD
Scenario 2 (0.25°)		
Period	Selected Inputs	Method
(1980.01.01-1999.12.31)	ERA5L/ GLDAS20/ GLEAMv3.7a	EIVD
(2000.01.01-2022.12.31)	ERA5L/ GLDAS21/ GLEAMv3.7a	

487 It should be noted that the same product can have different versions. In this study,

488 appropriate versions are selected based on the following principles: (1) Selection
 489 based on the corresponding data coverage duration and ensuring more products to
 490 gain more information; (2) Choosing the latest version while considering the
 491 assumption of non-zero ECC conditions; (3) Making efforts to select the exact
 492 product versions for different periods, to avoid uncertainties caused by version
 493 changes. We selected a subset of sites to compare the fusion results using different
 494 versions, and the corresponding details will be presented in the discussion section.

495 3.6. Evaluation indices

496 Five statistical indicators, namely Root-mean-squared-error (*RMSE*), Pearson's
 497 correlation coefficient (*R*), Mean-absolute-error (*MAE*), unbiased *RMSE* (*ubRMSE*)
 498 and Kling-Gupta Efficiency (*KGE*), are selected for comparison with existing
 499 products. The relative equations are shown as follows:

$$RMSE = \sqrt{\frac{\sum_{i=1}^n (sim_i - obs_i)^2}{n}} \quad (23)$$

$$R = \frac{\sum_{i=1}^n (sim_i - \overline{sim})(obs_i - \overline{obs})}{\sqrt{\sum_{i=1}^n (sim_i - \overline{sim})^2 \sum_{i=1}^n (obs_i - \overline{obs})^2}} \quad (24)$$

$$-1 \leq R \leq 1$$

$$MAE = \frac{1}{n} \sum_{i=1}^n |sim_i - obs_i| \quad (25)$$

$$ubRMSE = \sqrt{\frac{\sum_{i=1}^n [(sim_i - \overline{sim}) - (obs_i - \overline{obs})]^2}{n}} \quad (26)$$

500 Where *sim* is the simulations, *obs* is the observation as reference.

501 The modified *KGE* (Kling et al., 2012) offers insights into reproducing temporal
 502 dynamics and preserving the distribution of time series, which are increasingly used
 503 to calibrate and evaluate hydrological models (Knoben et al., 2019). For a better
 504 understanding of the *KGE* statistic and its advantages over the Nash-Sutcliffe
 505 Efficiency (*NSE*), please refer to Gupta et al. (2009). The equation is given by:

$$KGE = 1 - \sqrt{(r - 1)^2 + \left(\frac{\sigma_{sim}}{\sigma_{obs}} - 1\right)^2 + \left(\frac{\sigma_{sim}/\mu_{sim}}{\sigma_{obs}/\mu_{obs}} - 1\right)^2} \quad (27)$$

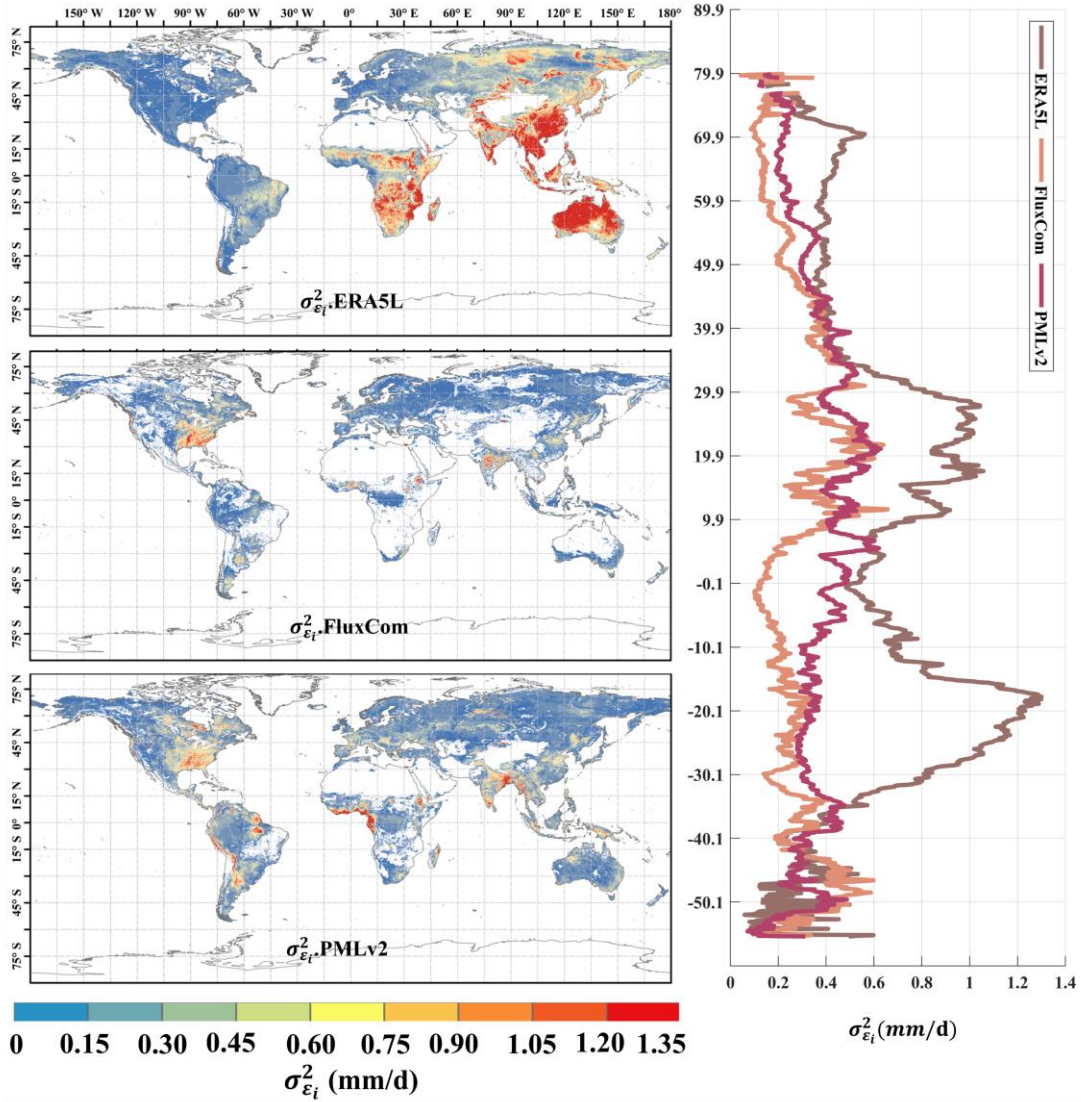
506 Where σ_{obs} and σ_{sim} are the standard deviations of observations and simulations;
 507 μ_{obs} and μ_{sim} are the mean of observations and simulations. Similar to *NSE*, $KGE = 1$
 508 indicates perfect agreement of simulations, while $KGE < 0$ reveals that the average of
 509 observations is better than simulations (Towner et al., 2019).

510 **4. Results**

511 In this study, we aimed to compare and evaluate the performance of fused products at
 512 both site and global scales. At the site scale, the performance of the fused products
 513 was evaluated against 212 FluxNet observations and compared with other products,
 514 including the simple average. At the global scale, the mean and temporal variations of
 515 the land surface ET calculated by the fused products were compared with those of
 516 other products.

517 **4.1. Analysis of error variances and weights**

518 This section examines the random error variances and identifies the predominant
 519 product based on assigned weights for the 0.1° and 0.25° inputs obtained through the
 520 EIVD method.



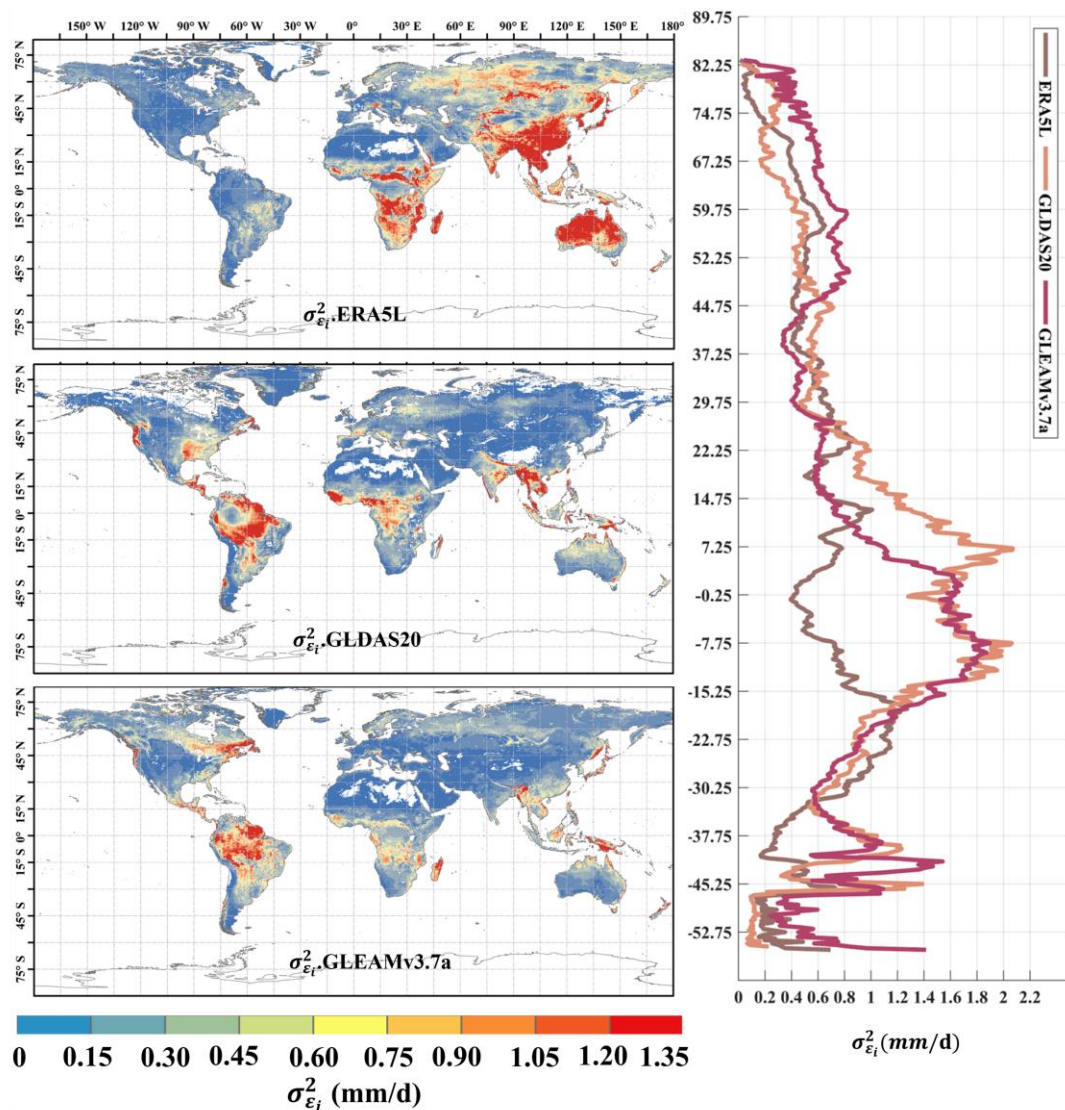
521

522 **Figure 2** Global distribution of absolute error variances ($\sigma_{\epsilon_i}^2$) of ERA5L, FluxCom,
 523 and PMLv2 using EIVD at 0.1° from 2001 to 2015, depicted alongside corresponding
 524 variation curves of average $\sigma_{\epsilon_i}^2$ with latitude.

525 **Figure 2** represents the random errors of the correlation products calculated using the
 526 EIVD method from 2001 to 2015 at 0.1° , where a non-zero ECC is assumed between
 527 FluxCom and PMLv2. The areas with missing values are due to the absence of data
 528 from either FluxCom or PMLv2 in those regions. The global random error variances
 529 (mean \pm standard deviation) obtained using the EIVD method are as follows: ERA5L:
 530 0.58 ± 0.53 mm/day, FluxCom: 0.12 ± 0.13 mm/day, PMLv2: 0.17 ± 0.14 mm/day.
 531 These results indicate that FluxCom performs best overall, while ERA5L performs the
 532 poorest. Regarding spatial distribution, regions with more significant random errors in

533 ERA5L are mainly located in East Asia, Australia, and southern Africa. On the other
534 hand, FluxCom and PMLv2 show relatively more considerable uncertainties in the
535 southeastern United States. The latitude distribution reveals that ERA5L has the
536 highest uncertainty, primarily in the vicinity of 20° to 30° north and south, consistent
537 with its spatial distribution.

538 It is important to note that due to missing data in specific regions at 0.1°, such as
539 Northern Africa, the Sahara Desert region, Northwestern China, and Australia, the
540 error results obtained may not accurately reflect the performance of FluxCom and
541 PMLv2 in these areas. Considering the current results, we can cautiously conclude
542 that FluxCom and PMLv2 demonstrate better performance. Future data
543 supplementation in these regions would further enhance our ability to analyze the
544 products' accuracy.

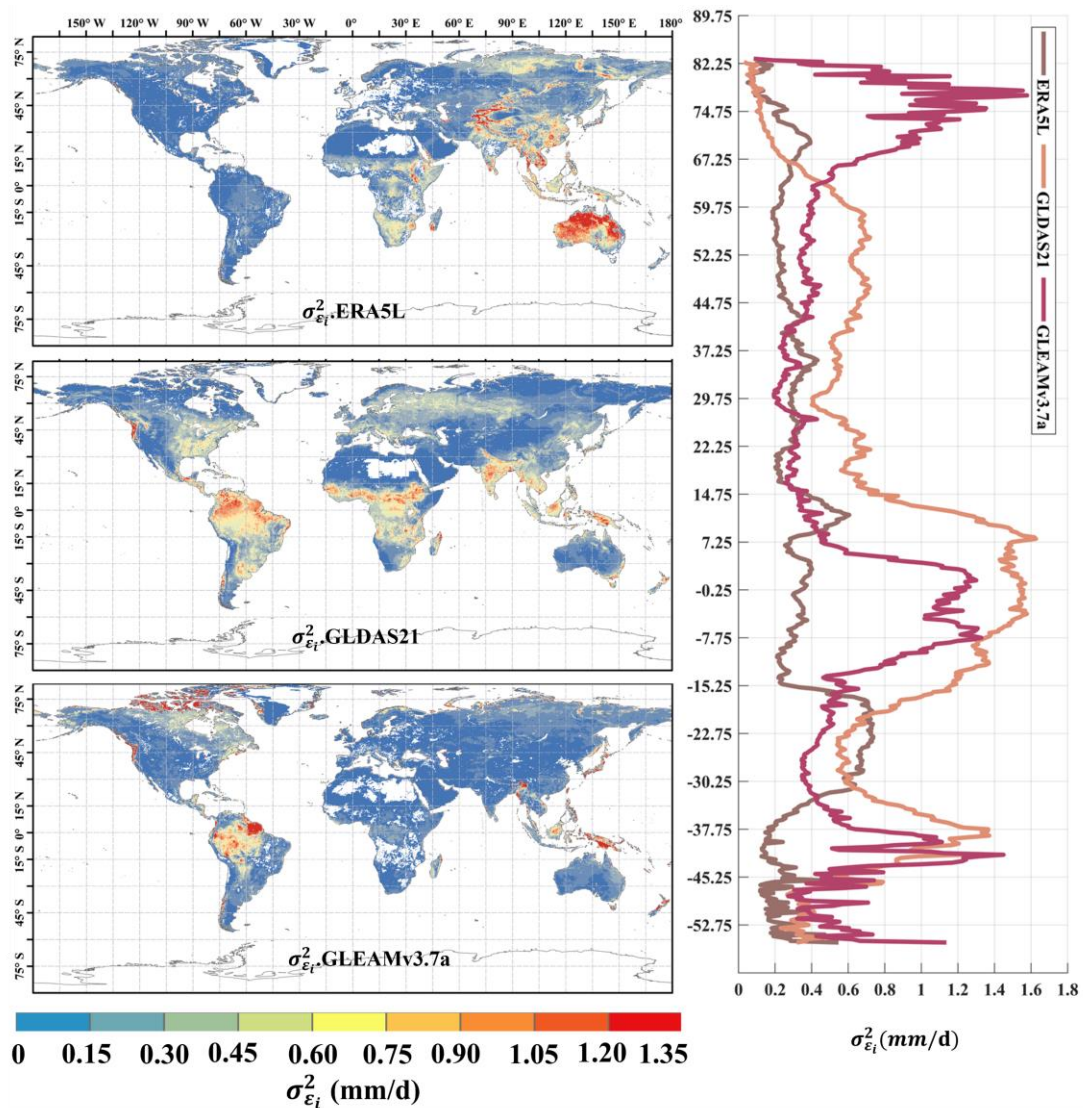


545

546 **Figure 3** Global distribution of absolute error variances ($\sigma_{\epsilon_i}^2$) of ERA5L, GLDAS2.0,
 547 and GLEAMv3.7a using EIVD at 0.25° from 1980 to 1999, depicted alongside
 548 corresponding variation curves of average with latitude.

549 The distribution of random error variance for ERA5L (0.59 ± 0.58 mm/d), GLDAS2.0
 550 (0.37 ± 0.44 mm/d), and GLEAMv3.7a (0.38 ± 0.36 mm/d) from 1980 to 1999 at 0.25°
 551 is shown in **Figure 3**. Here, we assumed a non-zero ECC between ERA5L and
 552 GLEAM. The ERA5L data was resampled from a 0.1° resolution to 0.25° , and its
 553 error distribution pattern is like that of the 0.1° resolution. It exhibits higher
 554 uncertainties in East Asia, Australia, and southern Africa. GLDAS and GLEAM
 555 exhibit relatively higher uncertainty over the southeastern United States and the
 556 Amazon Plain. GLDAS and GLEAM show similar performance among the three

557 products, while ERA5L performs relatively worse. Regarding the average distribution
 558 with latitude, ERA5L demonstrates a more even distribution, whereas GLDAS and
 559 GLEAM exhibit relatively higher uncertainties in tropical regions.
 560 The ET calculations in both GLDAS and GLEAM involve complex surface
 561 parameterization processes. In tropical regions, the high non-heterogeneity in land
 562 covers poses a challenge, and the 0.25° resolution grid may not capture the intricacies
 563 of the underlying surface conditions. This mismatch could impact the
 564 parameterization process, leading to errors. Future work could involve in-depth model
 565 analyses or sensitivity experiments to identify sources of error in complex ET models,
 566 facilitating improvements.



567

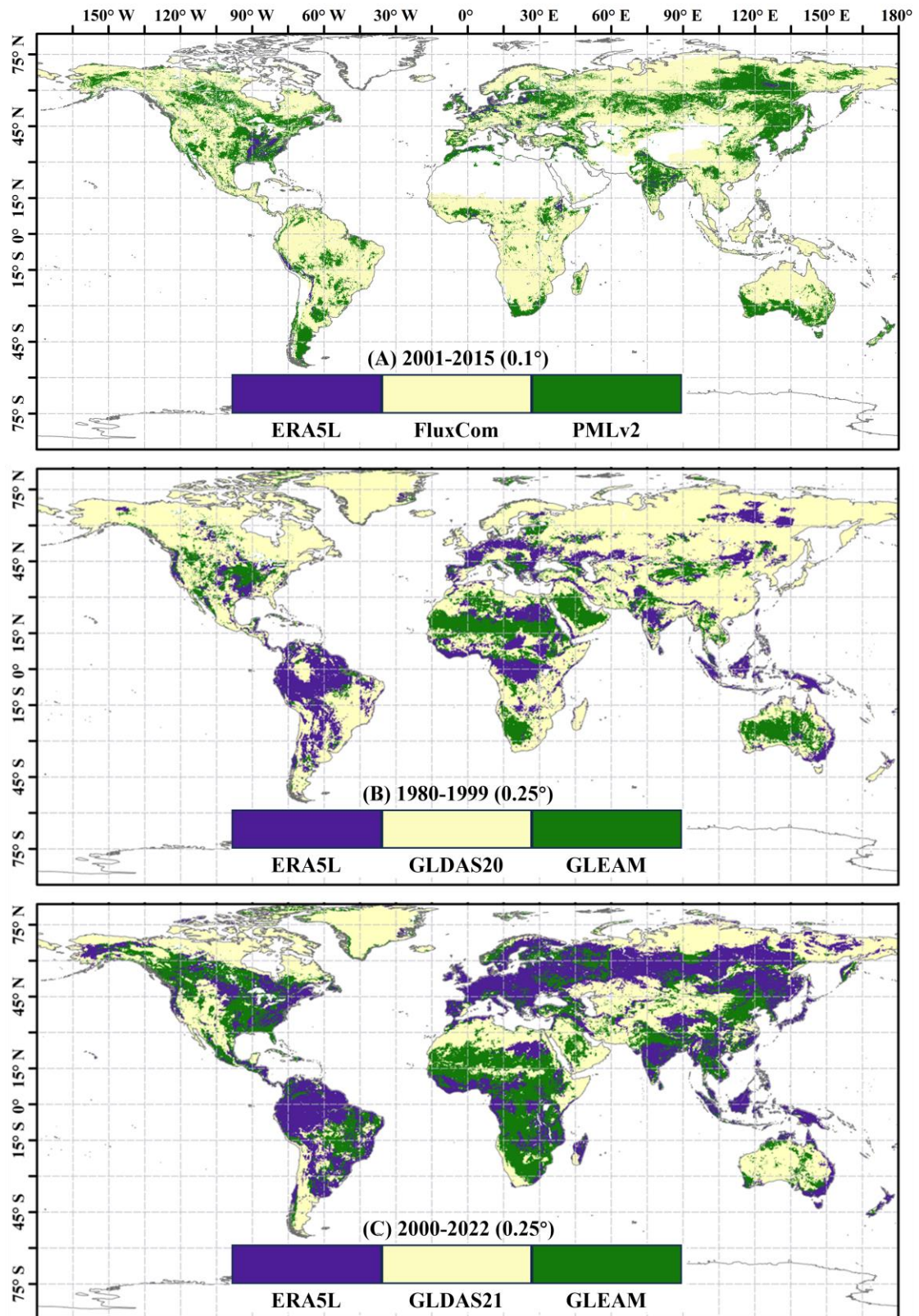
568 **Figure 4** Global distribution of absolute error variances ($\sigma_{\epsilon_i}^2$) of ERA5L, GLDAS2.1,

569 and GLEAMv3.7a using EIVD at 0.25° from 2000 to 2022, depicted alongside
570 corresponding variation curves of average with latitude.

571 In addition, **Figure 4** presents the distribution of random error variance for ERA5L
572 (0.32 ± 0.33 mm/d), GLDAS2.1 (0.35 ± 0.29 mm/d), and GLEAMv3.7a (0.38 ± 0.36
573 mm/d) from 2000 to 2022 at a resolution of 0.25° . The non-zero ECC assumption was
574 made between ERA5L and GLEAM. In this combination, ERA5L shows significantly
575 lower errors than in previous periods, indicating improved ERA5L performance
576 during this time frame. However, ERA5L still exhibits more significant errors in the
577 East Asia and Australia regions compared to the other two datasets. The overall errors
578 for GLDAS and GLEAM have also decreased, but there are still random error
579 variances exceeding 1.0 mm/d in the Amazon plain and Indonesia region. Regarding
580 the latitudinal distribution, ERA5L shows relatively smooth changes, while GLDAS
581 and GLEAM exhibit similar trends. However, GLEAM demonstrates a noticeable
582 increase in errors near the Arctic.

583 Next, in **Figure 5**, we present the dominant product for each grid cell in the three
584 scenarios, where dominance refers to the product with the highest assigned weight.
585 The results in **Figure 5** indicate that at 0.1° resolution, the weights for FluxCom and
586 PMLv2 are significantly higher than ERA5L, aligning with the error calculations
587 presented in **Figure 2**. This underscores the effectiveness of error and weight analysis
588 based on collocation in reflecting product performance, thereby allowing for a rational
589 adaptation of weights. At 0.25° resolution, the dominant regions for ERA5L,
590 GLDAS-2, and GLEAM products are relatively balanced. In the fusion scenario from
591 1980 to 1999, GLDAS20 predominantly covers the Northern Hemisphere, while
592 GLEAM dominates the Southern Hemisphere, with ERA5L prevalent in the Amazon
593 region. However, in the fusion scenario from 2000 to 2022, GLEAM's dominant
594 region significantly expanded, primarily covering the central United States and
595 southeastern China. The Amazon region continues to be dominated by ERA5L. The
596 variation in dominant products highlights that the calculation of product weights

597 evolves with changes in the fusion scenario. The error and weight computation
598 methods based on collocation can only provide the minimum MSE solution for a
599 given combination of inputs. It is important to note that changes in inputs will impact
600 the results.



601

602 **Figure 5** Map of the prevailing product at individual pixels based on scenario-specific

603

weights.

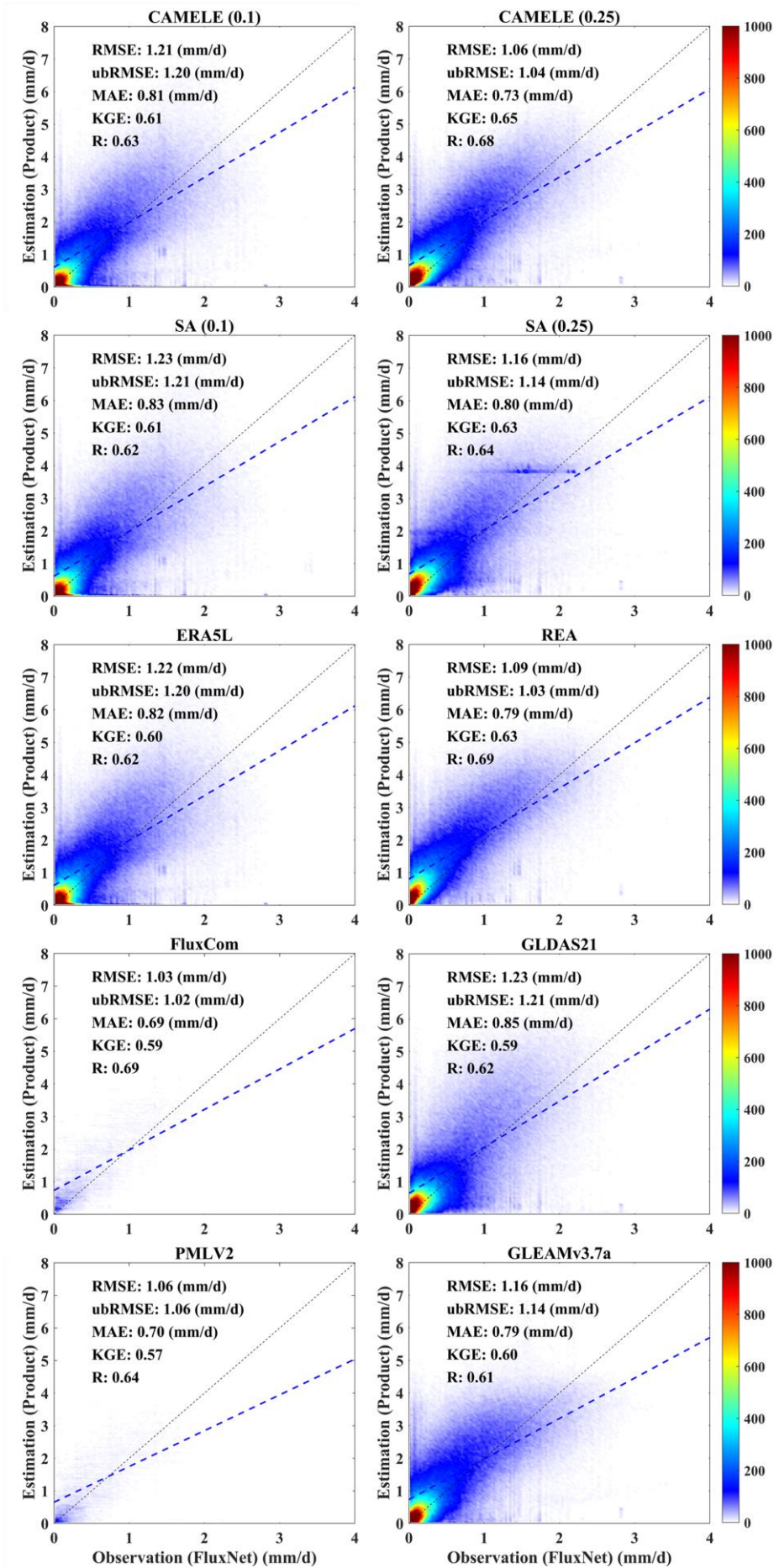
604

For the analysis at a resolution of 0.1°, we also applied the IVD method to calculate

605 the errors between ERA5L and PMLv2 for two time periods: 2000 and 2015 to 2020.
606 Since the analysis of product errors is not the focus of this paper, we provide the
607 results of the IVD in the appendix. Grids with higher random error variances
608 correspond to smaller weights when calculating the weights. The weight distribution
609 calculated at different time intervals is available in the appendix.

610 **4.2. Site-scale evaluation and comparison**

611 At the site scale, the performance of CAMELE was compared with FluxNet as the
612 reference. In this subsection, **Figure 6** and **Table 3** correspond to each other, as they
613 integrate data from 212 sites for all available periods, allowing for a comparative
614 analysis of the performance of different products at different times. Similarly, **Figure**
615 **7** and **Table 4** correspond to each other, where different product metrics were
616 calculated for each site, and the calculated metric results were subjected to statistical
617 analysis.



619 **Figure 6** Scatter plots of product corresponding to the available period data from 212
620 FluxNet sites. The colorbar represents the density, with darker colors indicating
621 higher concentration. The left and right columns present results for 0.1° and 0.25°
622 resolutions, respectively, with "SA" indicating the results for simple average.
623 Relevant statistical metrics are annotated in their respective figures.

624 The scatter plots in **Figure 6** demonstrate that CAMELE consistently performs at 0.1°
625 and 0.25° resolutions. At 0.1° resolution, FluxCom and PMLv2 showed superior
626 performance with fewer data points due to their original 8-day average resolution.
627 CAMELE exhibited a performance like ERA5L. At 0.25° resolution, CAMELE
628 performed comparably to the other datasets, demonstrating reasonable accuracy.
629 Notably, there was an improvement in the KGE and R indices. The fitted line closely
630 approximated the 1:1 line, indicating a solid agreement with the observed values.
631 Moreover, the results obtained from the simple average were also acceptable, but SA
632 (0.25°) had a concentration of data points between (2-4 mm/d), possibly due to the
633 inputs having a high concentration within that range. The assumption that a simple
634 average implies equal performance of each product on every grid cell is inaccurate;
635 variations in performance exist among different products across distinct grid cells
636 (regions).

637 **Table 3** Average values of different metrics for CAMELE and other fusion schemes
638 corresponding to the available period data from 212 FluxNet sites. The bolded
639 sections indicate the schemes with the best performance in their respective metrics.

	Product	RMSE (mm/d)	ubRMSE (mm/d)	MAE (mm/d)	KGE	R
0.1°-daily	CAMELE	1.21	1.20	0.81	0.61	0.63
	SA	1.23	1.21	0.83	0.61	0.62
	ERA5L	1.22	1.20	0.82	0.60	0.62
	FluxCom	1.03	1.02	0.69	0.59	0.69
	PMLv2	1.06	1.06	0.70	0.57	0.64
0.25°-daily	CAMELE	1.06	1.04	0.73	0.65	0.68
	SA	1.16	1.14	0.80	0.63	0.64

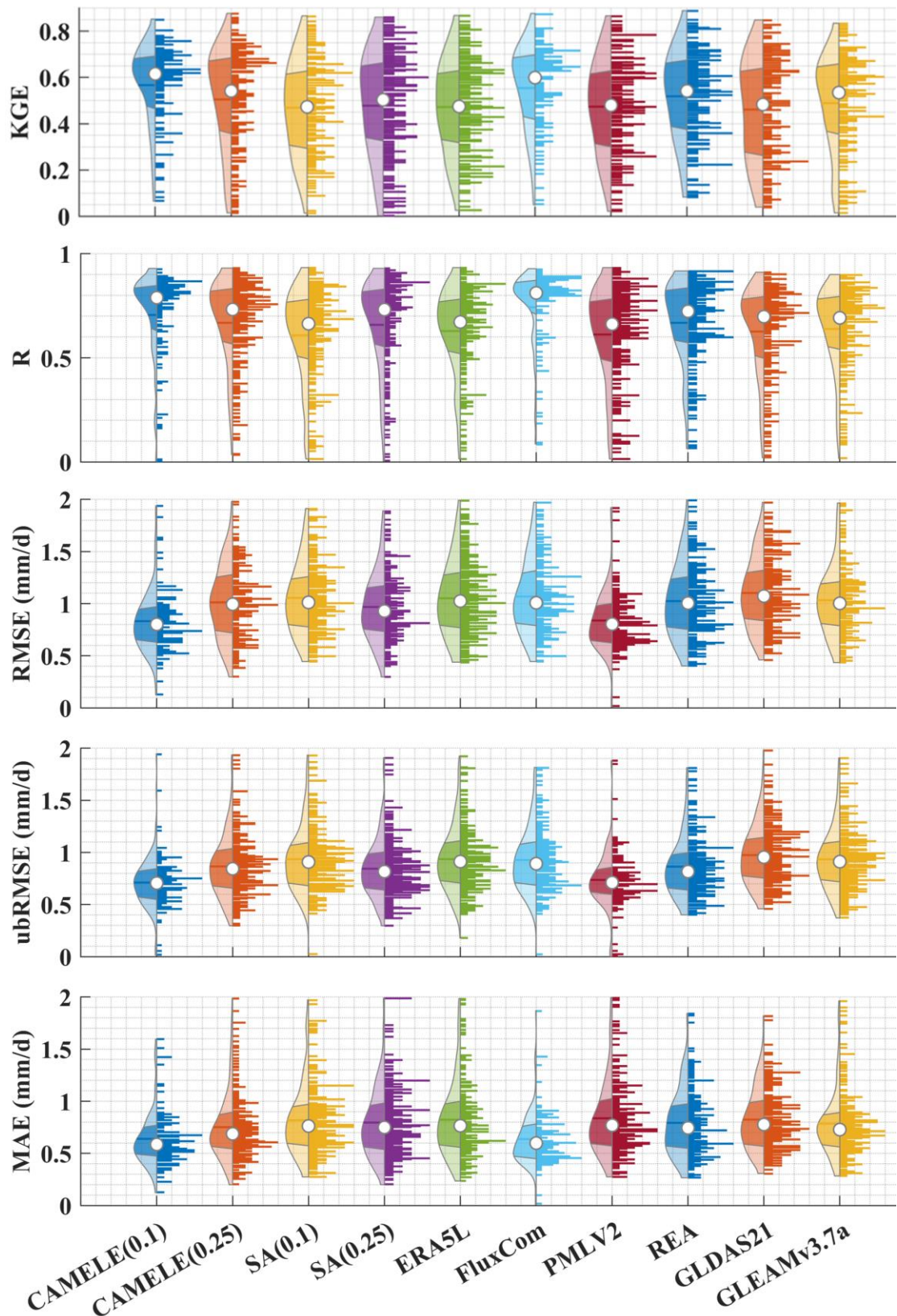
REA	1.09	1.03	0.79	0.63	0.69
GLDAS21	1.23	1.21	0.85	0.59	0.62
GLEAMv3.7a	1.16	1.14	0.79	0.60	0.61

640 The information in **Table 3** corresponds to **Figure 6** and presents the results of
641 various product indicators. The bolded parts indicate the products with the best
642 corresponding indicators. The results indicate that CAMELE performed well at both
643 0.1° and 0.25° resolutions, mainly showing improvements in the KGE and R
644 indicators. FluxCom exhibited the best performance; however, considering that this
645 product utilized FluxNet sites for result calibration, this phenomenon is reasonable. In
646 this study, we pooled the data from all 212 available periods at the stations as a
647 reference without considering the differences between individual sites. This approach
648 provided an initial validation of the reliability of CAMELE at all sites.

649 The information in **Figure 7** corresponds to the data presented in **Table 4**, which
650 involves the calculation of five indicators at each site, followed by statistical analysis
651 of these indicators. From the distribution of the violin plots, it can be observed that a
652 violin plot with a closer belly to 1 indicates better results in terms of the R and KGE
653 indicators. CAMELE performs well overall, closely resembling PMLv2 and FluxCom.
654 On the other hand, the results obtained from the Simple Average are relatively poorer.
655 Regarding the RMSE, ubRMSE, and MAE indicators, a violin plot with a closer belly
656 to 0 suggests less errors. CAMELE demonstrates a notable enhancement in
657 performance at the 0.1° level. This suggests that the fusion method effectively reduces
658 errors, aligning with the original intention of weight calculation, and it compares
659 favorably with the products used in the merging scheme.

660 Additionally, FluxCom and PMLv2 also exhibit minimal errors, which is expected
661 considering their utilization of FluxNet sites for error correction. Furthermore, SA
662 shows significantly larger errors. Although the simple average method can
663 compensate for positive and negative errors between inputs in some instances, it can
664 also lead to error accumulation, as evidenced by the results in the violin plots.

665



666

667

Figure 7 Violin plots obtained by aggregating five different statistical indicators,

668

calculated separately for each site. In each violin plot, the left side represents the

669 distribution, with the shaded area indicating the box plot, the dot representing the
 670 mean, and the right side showing the histogram.

671 **Table 4** Average values of indicators corresponding to different products, calculated
 672 based on the comprehensive results obtained for each site. The bolded sections
 673 indicate the schemes with the best performance in their respective metrics.

	Product	RMSE (mm/d)	ubRMSE (mm/d)	MAE (mm/d)	KGE	R
0.1°-daily	CAMELE	0.83	0.71	0.64	0.57	0.71
	SA	1.05	0.93	0.82	0.47	0.61
	ERA5L	1.05	0.94	0.82	0.47	0.63
	FluxCom	1.07	0.93	0.64	0.55	0.74
	PMLv2	0.84	0.74	0.84	0.47	0.61
0.25°-daily	CAMELE	1.03	0.87	0.75	0.51	0.67
	SA	0.97	0.84	0.80	0.48	0.66
	REA	1.02	0.86	0.80	0.48	0.67
	GLDAS21	1.10	0.97	0.83	0.46	0.63
	GLEAMv3.7a	1.03	0.93	0.79	0.49	0.64

674 **Table 4** presents the average values of different metrics in **Figure 7**, boldly
 675 highlighting the optimal products corresponding to each metric. It can be observed
 676 that CAMELE exhibits significant improvements in performance at a resolution of
 677 0.1°, particularly in terms of the error metrics RMSE and ubRMSE, surpassing other
 678 products. This further confirms the effectiveness of our fusion scheme in reducing
 679 product errors. Additionally, although the performance of CAMELE at a resolution of
 680 0.25° is comparable to other products, there is still a slight decline compared to its
 681 performance at 0.1°. This can be attributed partly to the inherent errors in the input
 682 products and partly to the decreasing representativeness of FluxNet, which serves as
 683 the reference at the 0.25° grid. Nevertheless, we can still consider CAMELE to have
 684 good accuracy.



685

686

Figure 8 Heatmaps of five statistical indicators, where each row corresponds to the mean value for all sites of the specific PFT, and each column corresponds to a product.

687

688

The product with the best performance for that PFT is highlighted in bold within each

689

row. (a)-(c) represent three error indicators: RMSE, ubRMSE, and MAE; (d)-(e)

690

represent two goodness-of-fit indicators: KGE and R.

691

Table 5 Optimal product corresponding to different PFTs under various statistical indicators against observations from FluxNet sites

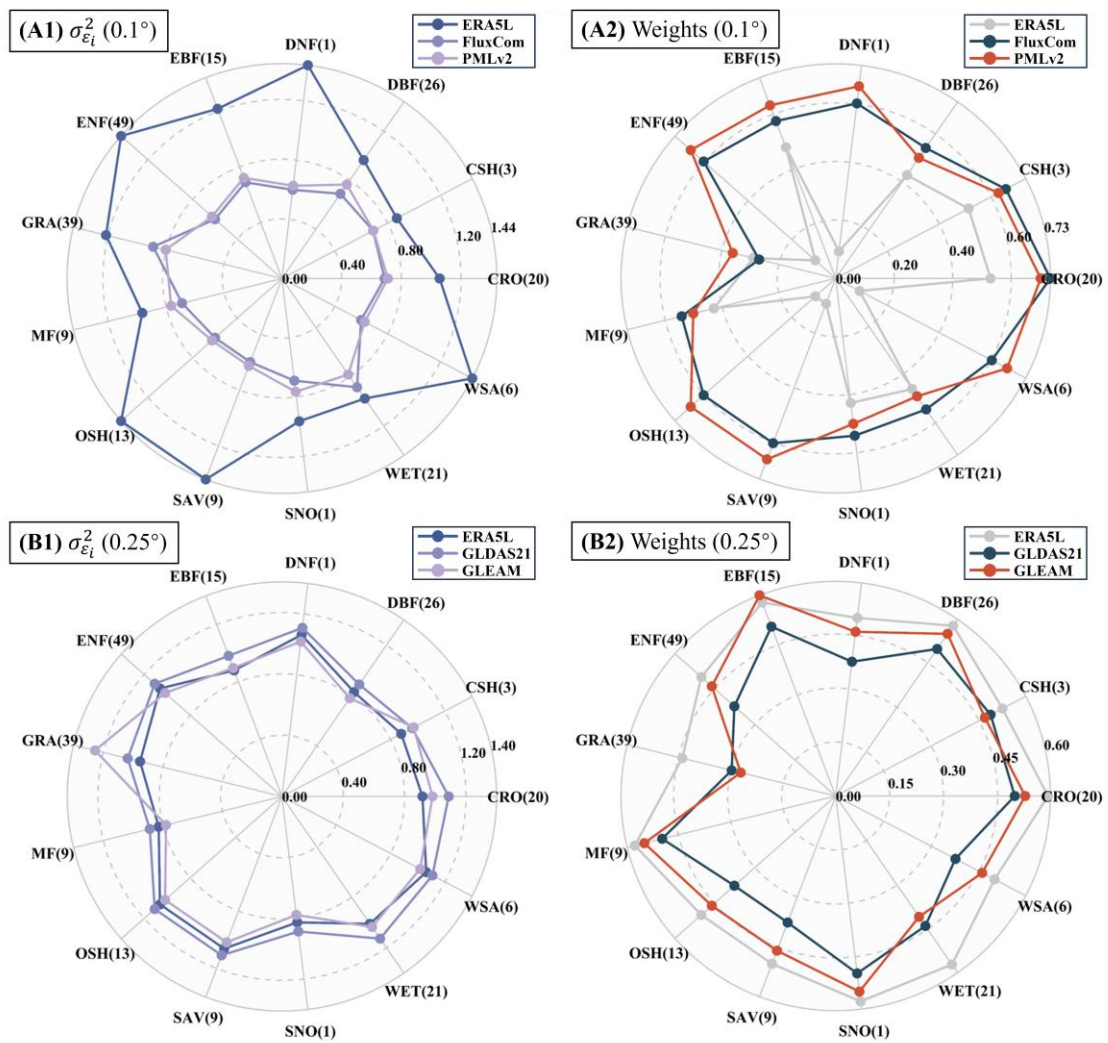
692

IGBP (n-sites)	RMSE (mm/d)	ubRMSE (mm/d)	MAE (mm/d)	KGE	R
<i>CRO</i> (20)	CAMELE	CAMELE	CAMELE	PMLv2	CAMELE

<i>CSH (3)</i>		PMLv2		FluxCom	FluxCom	
<i>DBF (26)</i>		CAMELE		REA		
<i>DNF (1)</i>				FluxCom		CAMELE
<i>EBF (15)</i>				CAMELE		GLEAM
<i>ENF (49)</i>				FluxCom		CAMELE
<i>GRA (39)</i>	PMLv2	CAMELE	FluxCom	CAMELE	CAMELE	
<i>MF (9)</i>	CAMELE	CAMELE	CAMELE	REA	FluxCom	
<i>OSH (13)</i>			FluxCom	CAMELE		
<i>SAV (9)</i>			CAMELE	REA		
<i>SNO (1)</i>			PMLv2	FluxCom		CAMELE
<i>WET (21)</i>			CAMELE	FluxCom		CAMELE
<i>WSA (6)</i>			CAMELE	FluxCom		CAMELE

693 Furthermore, we classified 212 sites according to PFTs and analyzed the statistical
694 indicators of different PFTs corresponding to each site. The results are represented in
695 **Figure 8** as a heatmap, and the corresponding optimal products for other PFTs sites
696 are marked in **Table 5**. The results show that CAMELE performs the best in almost
697 all PFTs categories, as indicated by various indicators. While on sites where other
698 products perform better, CAMELE's indicators are comparable to the optimal
699 products, albeit slightly inferior. This indicates that our fusion approach effectively
700 combines the advantages of different products, resulting in superior fusion results
701 across different vegetation types.

702 From the results, it is evident that CAMELE performs well across various vegetation
703 types. To delve deeper into the reasons behind this performance, we conduct site-scale
704 analyses at two resolutions, evaluating errors and computed weights for different
705 PFTs sites. These are visualized in radar chart format in **Figure 9**.



706

707 **Figure 9** Mean collocation-based errors and weights of different products at various
 708 PFTs sites at (A) 0.1° and (B) 0.25° resolutions. The parentheses next to each PFTs
 709 name denote the corresponding number of sites.

710 The results from **Figure 9** demonstrate that the error-weighting calculation method
 711 based on collocation effectively considers the error situation of inputs, thereby
 712 providing reasonable weight assignments. At 0.1° resolution, ERA5L's error is
 713 significantly higher across all PFTs than FluxCom and PMLv2, resulting in relatively
 714 lower corresponding weights. FluxCom and PMLv2 exhibit closer performance, with
 715 higher weights at most PFT sites. At 0.25° resolution, ERA5L, GLDAS21, and
 716 GLEAM perform more evenly, with minimal differences, resulting in closer weights.
 717 The weights for different inputs vary noticeably with changes in PFTs, depending on
 718 the performance of other products within the same combination. Products with more

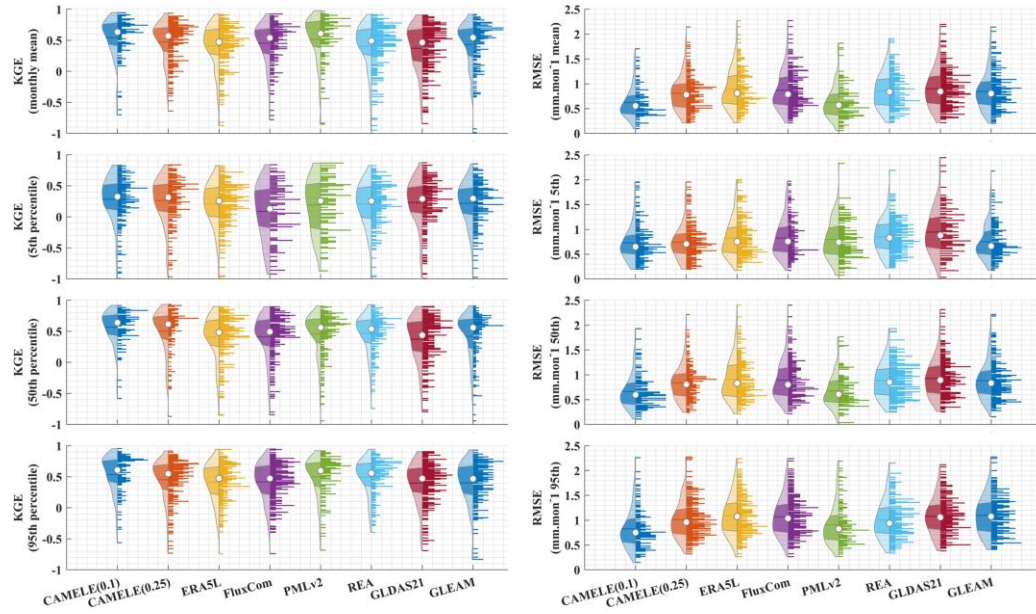
719 significant errors correspondingly have lower weights, affirming the rationale behind
720 the fusion method. However, it is essential to note that the presented results depict the
721 mean values of errors and weights across all sites; there might be variations among
722 sites with the same PFTs.

723 In summary, using the filtered daily-scale data from 212 FluxNet sites as a reference,
724 we conducted a benchmark analysis with CAMELE and demonstrated its good fit
725 with the observed data. Additionally, by comparing the performance of different
726 products at each site, we further illustrated that CAMELE exhibits similar or slightly
727 improved accuracy and minor errors compared to existing products.

728 **4.3. Assessment and comparison of multi-year average**

729 In this section, we will first analyze and compare the performance of CAMELE with
730 other products in estimating the multi-year mean and extreme values of ET at the site
731 scale. Subsequently, a global-scale analysis will be conducted for the same periods
732 (0.1°: 2001 to 2015; 0.25°: 2000 to 2017) to examine the distribution of multi-year
733 daily average ET calculated by different products. For site comparisons, we have
734 selected monthly mean ET values and three quantiles (5th, 50th, and 95th) to
735 represent the products' performance in estimating ET's average and extreme values.

736



737

738

739

740

741

742

743

744

745

Figure 10 Violin plots depicting the KGE and RMSE metrics calculated for CAMELE and other products based on the monthly mean, 5th, 50th, and 95th percentiles at each FluxNet site. The left four columns represent KGE plots, while the right four columns represent RMSE plots. The dots in the violin plots represent the median, and the horizontal lines represent the mean.

Table 6 Average values of KGE and RMSE corresponding to different products, calculated based on the results obtained for each site. The bolded sections indicate the schemes with the best performance in their respective metrics.

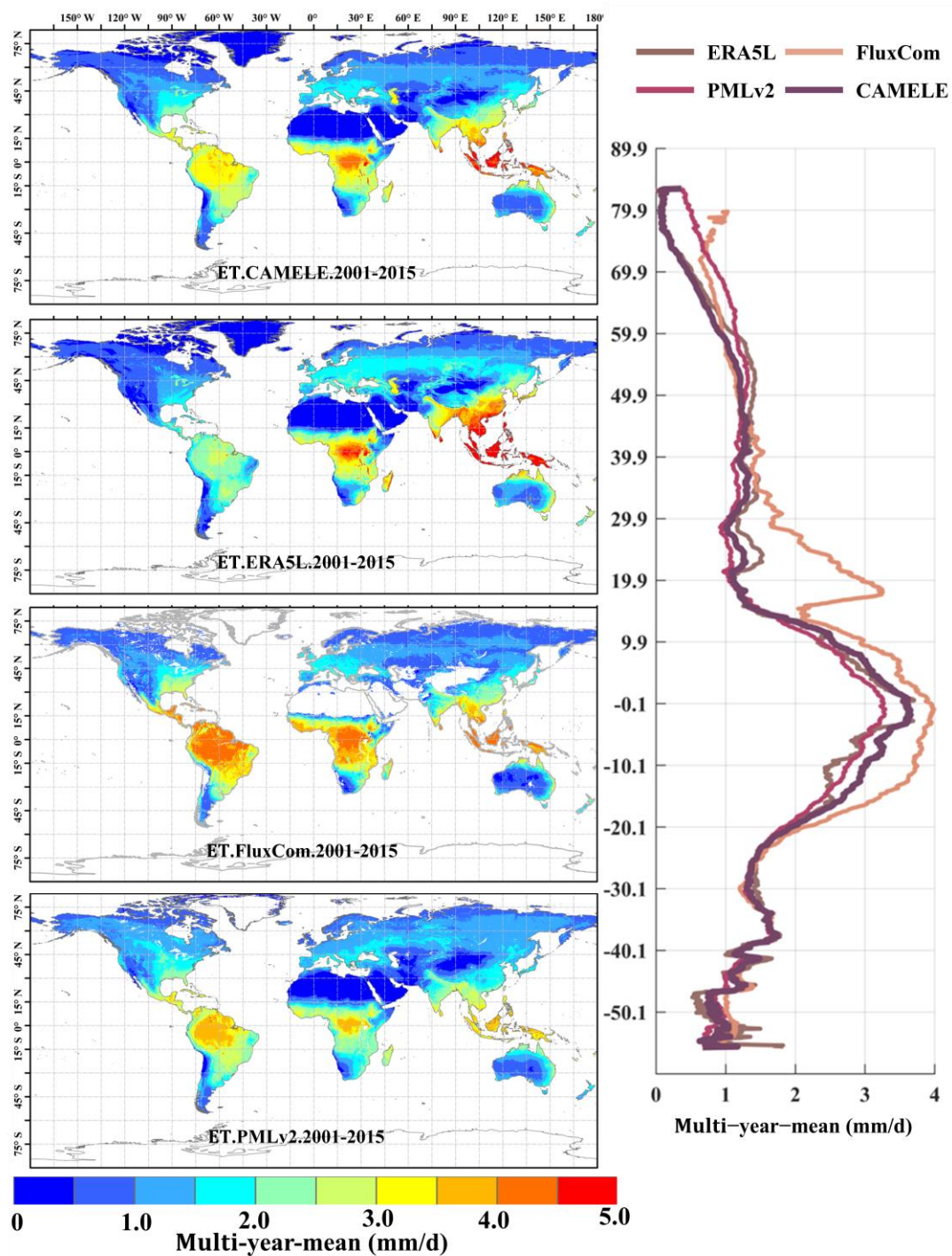
Product		KGE			
		Mean	5 th	50 th	95 th
0.1°-daily	CAMELE	0.54	0.28	0.57	0.54
	ERA5L	0.41	0.21	0.40	0.42
	FluxCom	0.45	0.09	0.42	0.42
	PMLv2	0.52	0.19	0.46	0.50
0.25°-daily	CAMELE	0.47	0.26	0.50	0.45
	REA	0.40	0.21	0.46	0.50
	GLDAS21	0.37	0.23	0.37	0.40
	GLEAMv3.7a	0.43	0.22	0.42	0.40
Product		RMSE (mm/mon)			
		Mean	5 th	50 th	95 th
0.1°-daily	CAMELE	0.63	0.73	0.66	0.83

	ERA5L	0.89	0.83	0.91	1.09
	FluxCom	0.87	0.83	0.89	1.07
	PMLv2	0.63	0.80	0.68	0.91
	CAMELE	0.81	0.74	0.84	1.01
0.25°-daily	REA	0.86	0.85	0.88	1.01
	GLDAS21	0.90	0.95	0.93	1.08
	GLEAMv3.7a	0.85	0.75	0.88	1.10

746 The information in **Figure 10** corresponds to the data presented in **Table 6**, which
747 involves the calculation of KGE and RMSE at each site, followed by statistical
748 analysis. From the distribution of the violin plots, it can be observed that a violin plot
749 with a closer belly to 1 indicates better results in terms of the KGE.

750 The results show that CAMELE outperforms other products in the estimation of
751 monthly averages and the 5th, 50th, and 95th percentiles at both 0.1° and 0.25°
752 resolutions. Its performance in capturing monthly averages is noteworthy, with a
753 noticeable improvement in the KGE and RMSE metrics relative to the inputs.
754 Examining the results for percentiles, CAMELE shows a relatively poorer estimation
755 for shallow values (5th percentile) but still demonstrates some improvement
756 compared to the input data, albeit influenced by input errors.

757 At 0.1°, PMLv2 and FluxCom perform just below the fusion result, aligning with the
758 previous error and weight analysis. At 0.25°, GLEAM and REA closely follow
759 CAMELE, with REA exhibiting slightly better estimation results for extremely high
760 values (95th percentile) than CAMELE. Despite this, the analysis results still indicate
761 that the products obtained reflect well the multi-year averages and extremes of ET,
762 holding promise as reliable products for analyzing ET variations.



763

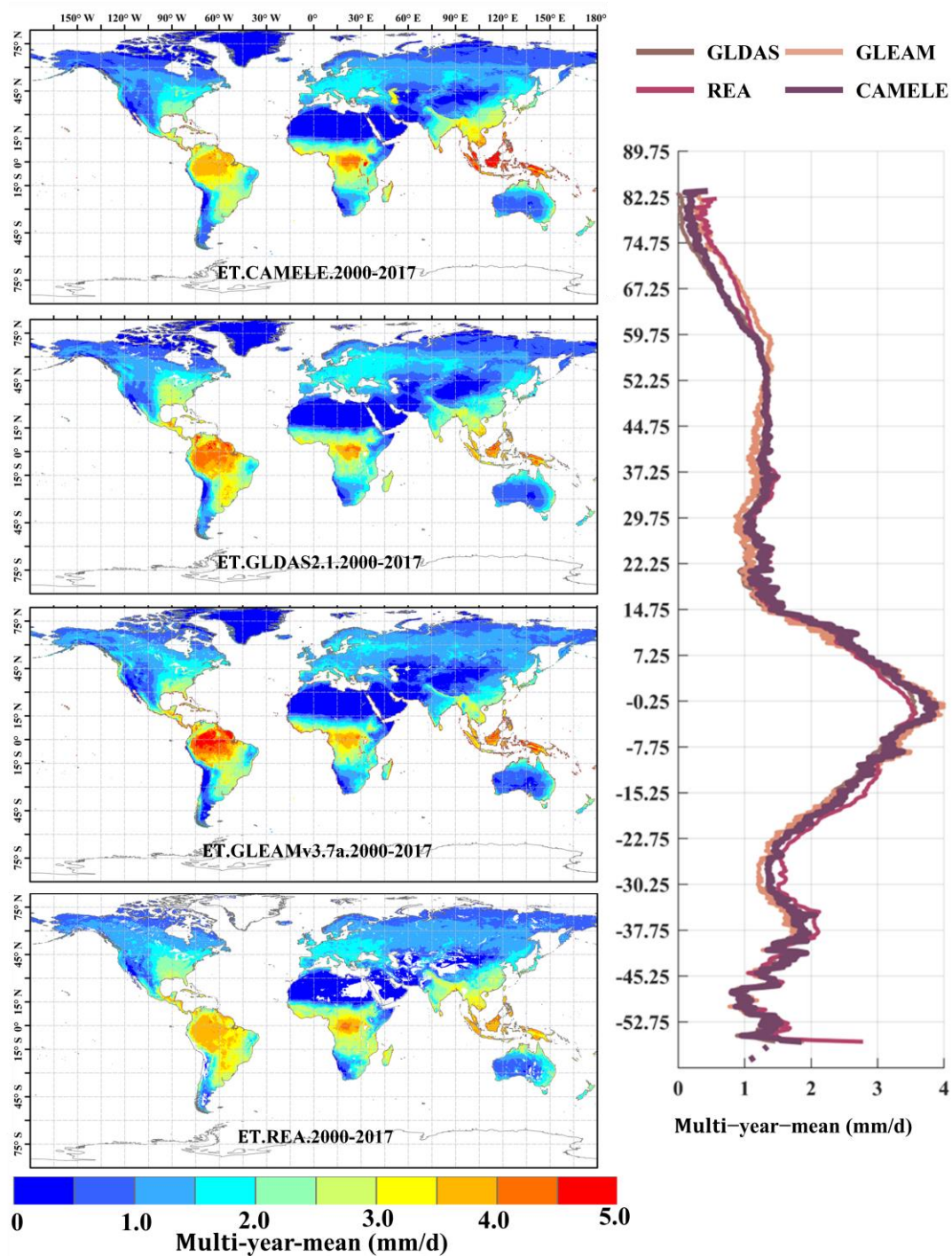
764 **Figure 11** Global distribution of multi-year daily average ET at 0.1° for CAMELE,
 765 ERA5L, FluxCom, and PMLv2, depicted alongside corresponding variation curves of
 766 multi-year daily average ET with latitude.

767 The results in **Figure 11** indicate significant differences in the multi-year daily
 768 average distribution of global evapotranspiration (ET) among different products.
 769 Specifically, ERA5L shows noticeably higher values in East Asia than other products,

770 while FluxCom and PMLv2 exhibit higher values in the Amazon rainforest and
771 southern Africa regions. This distribution pattern is consistent with the error results
772 obtained from the EIVD calculation, indicating that these products possess certain
773 uncertainties in the regions. In terms of the latitudinal distribution pattern, except for
774 FluxCom, which displays distinct fluctuations, the variability among the other
775 products is relatively similar. This suggests that despite spatial differences among the
776 different products, they maintain consistency in the overall quantity.

777 **Figure 12** presents the results with a resolution of 0.25° . It can be observed that
778 compared to the 0.1° distribution, the spatial distribution of annual average
779 evapotranspiration (ET) is more consistent among different products at 0.25° ,
780 showing larger ET values in tropical regions. The main differences are concentrated
781 in the Amazon rainforest and the Congo Basin, where GLEAM and GLDAS results
782 are higher than REA's. The assigned weights for REA's inputs (MERRA2, GLDAS,
783 and GLEAM.) are approximately equal in these two regions, each contributing about
784 one-third to the overall calculation (Lu et al., 2021). This balanced allocation results
785 in the REA being distributed among them roughly equally over multiple years in these
786 two regions. The latitude variation plots show that the results from each product are
787 very close, providing additional evidence for the reliability of CAMELE.

788



789

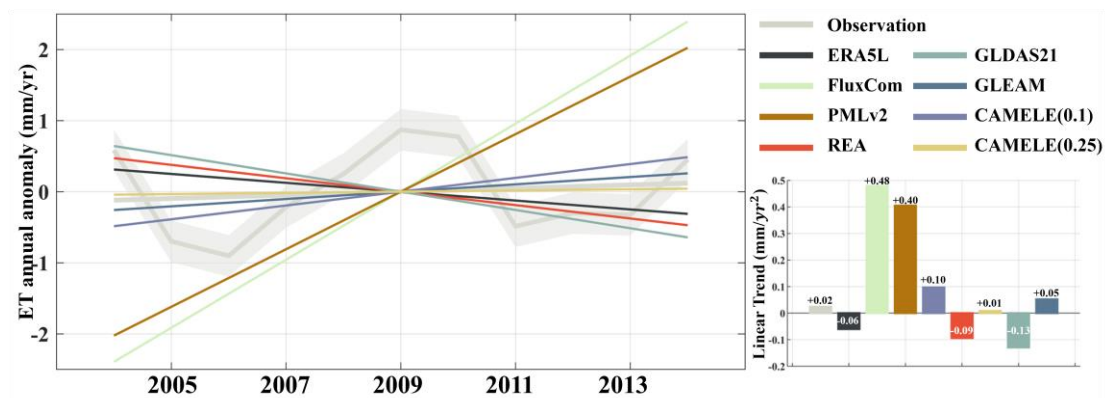
790 **Figure 12** Global distribution of multi-year daily average ET at 0.25° for CAMELE,
 791 GLDAS2.1, GLEAMv3.7a, and REA, depicted alongside corresponding variation
 792 curves of multi-year daily average ET with latitude.

793 In parallel, it is worth noting that, despite the regional disparities that may arise when
 794 contrasting the trends by CAMELE with inputs, a noteworthy consistency emerges
 795 when examining these trends along latitudinal gradients. This notable alignment

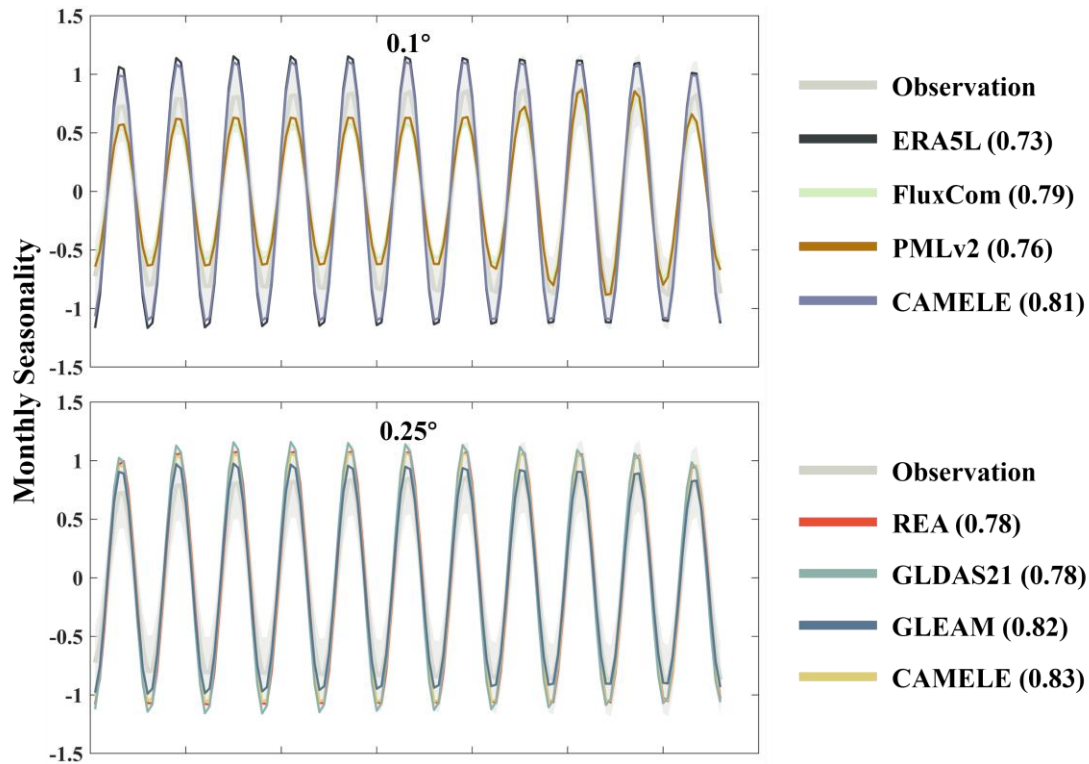
796 signifies the robustness of CAMELE to some extent. It underscores the capacity of
 797 CAMELE to capture ET patterns, providing further insights for the scientific
 798 community.

799 **4.4. Assessment and comparison of linear trend and seasonality**

800 In this section, we first validate and compare the performance of CAMELE with other
 801 products in estimating multi-year trends and seasonality at the site scale. Due to the
 802 inconsistent time lengths of FluxNet sites, trends at many sites are not significant.
 803 Therefore, we deliberately selected 13 sites with continuous evapotranspiration (ET)
 804 observations for the same 11-year period (2004 to 2014) and with significant trends.
 805 The annual ET values for each year were calculated as the mean of the 13 sites for
 806 that year, allowing the computation of linear trends and seasonality. We employed
 807 singular spectrum analysis (SSA), which assumes an additive decomposition $A = LT$
 808 $+ ST + R$. In this decomposition, LT represents the long-term trend in the data, ST is
 809 the seasonal or oscillatory trend (or trends), and R is the remainder.



810
 811 **Figure 13** Comparison of linear trend from 2004 to 2014 among 13 FluxNet sites
 812 using CAMELE and other products. The trends have been subjected to SSA
 813 decomposition, removing seasonality. The gray enveloping line represents the mean
 814 plus the standard deviation of the 13 sites.



815

816 **Figure 14** Comparison of seasonal variations from 2004 to 2014 among 13 FluxNet
 817 sites using CAMELE and other products. The seasonality has been obtained through
 818 SSA decomposition, with the gray area representing the observed values. The
 819 parentheses in each product name indicate the KGE coefficient comparing with the
 820 observed values.

821 In **Figure 13** and **Figure 14**, based on observations from FluxNet sites, we analyzed
 822 the performance of CAMELE and other products in estimating the linear trend and
 823 seasonality of ET over multiple years. It is important to note that we only present the
 824 analysis results for 13 sites with continuous 11-year observations, and the
 825 performance of different ET products in trend estimation at individual sites still varies,
 826 not fully reflecting the overall performance on all grids in terms of trend and
 827 seasonality. Nevertheless, such a comparison can still provide valuable insights.

828 Examining the results of the linear trend, both PMLv2 and FluxCom exhibit a
 829 significant upward trend, well above the observations. On the contrary, ERA5L,
 830 GLDAS, and REA show a noticeable downward trend, while CAMELE demonstrates
 831 a gradual upward trend closer to the observations. Additionally, GLEAM slightly

832 outperforming CAMELE at a resolution of 0.25°. Overall, CAMELE shows good
833 agreement with site observations in capturing the multi-year linear trend of ET.
834 Continuing with the analysis of seasonality, the KGE index comparing each product's
835 results with observed values is provided in parentheses next to the product name.
836 Generally, all products exhibit a good representation of ET's seasonal variations.
837 CAMELE's 0.1° seasonal results closely match FluxCom (with the two lines almost
838 overlapping). However, the fluctuations it reflects are higher than the observed values.
839 This is likely due to keeping the 8-day average results of FluxCom consistent with
840 PMLv2 every 8 days, and the variability in ET primarily originates from ERA5L
841 results. This aspect may need improvement in subsequent research. At 0.25°,
842 CAMELE's seasonal representation is closer to the observed results. The differences
843 in CAMELE's performance at the two resolutions are mainly attributed to input
844 variations, which we discuss in the following section as potential areas for
845 improvement.

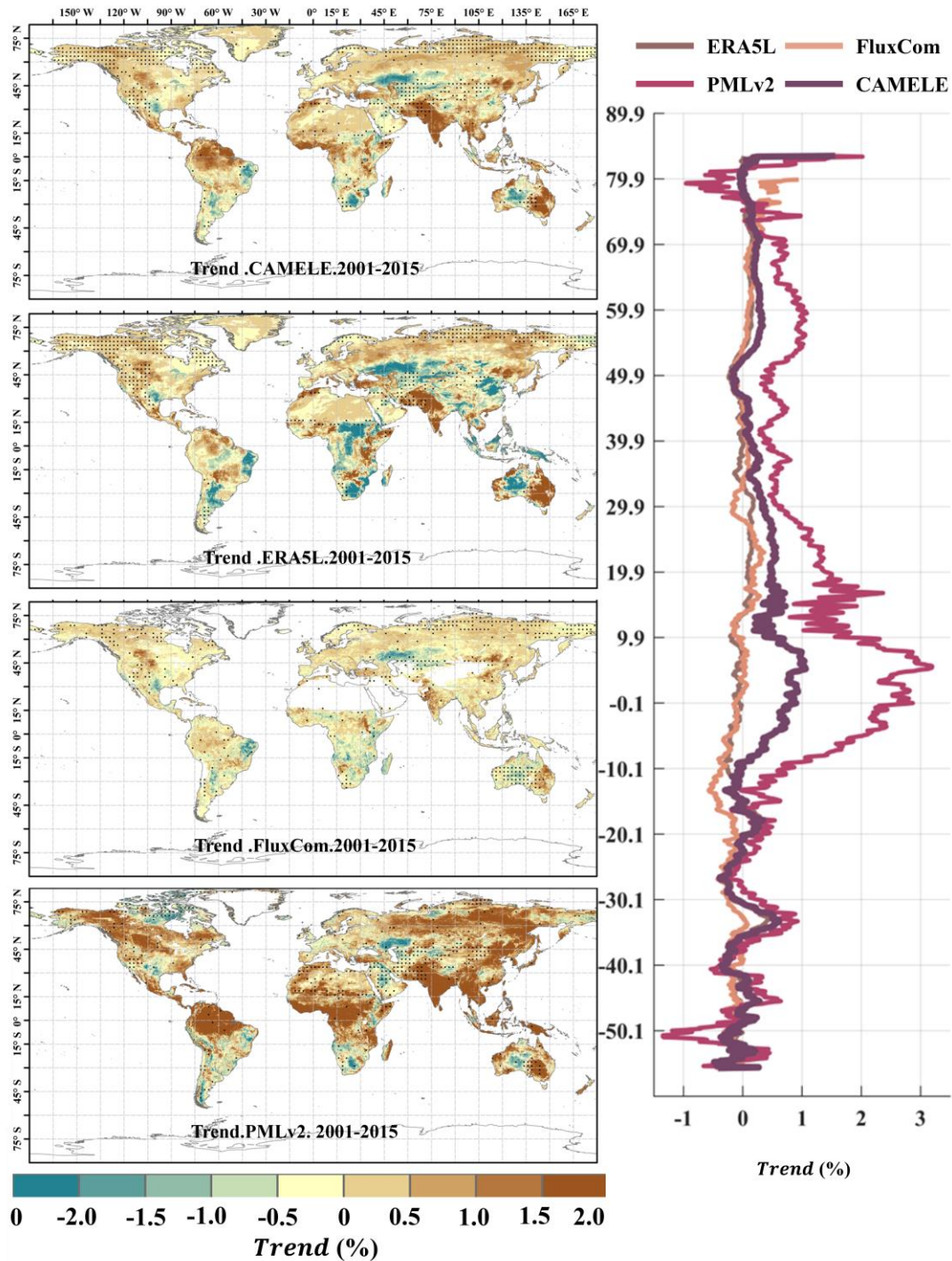
846 **Table 7** Comparison of CAMELE results at 13 continuous 10-year observational sites:
847 (a) Comparison of Linear trend; (b) KGE values for monthly seasonality.

Site Name	Observation	(a) Linear Trend (mm/yr) (2004-2014)		(b) KGE of seasonality	
		CAMELE (0.1)	CAMELE (0.25)	CAMELE (0.1)	CAMELE (0.25)
BE_Lon	0.15	0.06	0.05	0.65	0.71
CH_Lae	-0.33	-0.36	-0.35	0.80	0.80
CH_Oe2	0.25	0.37	0.67	0.85	0.49
CZ_BK1	-0.44	-0.53	-0.66	0.54	0.71
DE_Gri	0.11	0.03	0.24	0.61	0.54
DE_Kli	0.68	0.77	0.85	0.78	0.52
FR_Gri	0.41	0.36	0.55	0.71	0.55
GF_Guy	-0.47	-0.50	-0.45	0.77	0.73
IT_BCi	0.21	0.25	0.28	0.61	0.56
IT_NoE	0.11	0.02	0.04	0.61	0.51
US_GLE	-0.14	-0.17	-0.01	0.64	0.49
US_SRM	-0.42	-0.45	-0.63	0.52	0.61

ZM_Mon	0.16	0.22	0.09	0.56	0.51
--------	------	------	------	------	------

848 Furthermore, we present the linear trend estimated by CAMELE from 2004 to 2014 at
849 13 sites, along with the KGE values for monthly seasonality. The results indicate that
850 regardless of the resolution, whether 0.1° or 0.25° , the trends estimated by CAMELE
851 are consistent with the observed trends, with minor difference. In comparison to the
852 observed monthly seasonality, the KGE values exceed 0.5 at all sites, with some sites
853 exceeding 0.7, indicating that CAMELE can effectively capture the seasonal
854 variations.

855 The results indicate that CAMELE effectively captures the multi-year changes in ET,
856 but at 0.1° , it tends to overestimate seasonal fluctuations. We further generated global
857 maps of multi-year linear trends in ET, estimating trends using Theil–Sen's slope
858 method and testing significance with the Mann–Kendall method. The dotted areas
859 indicate trends passing a significance test at a 5% level.



860

861 **Figure 15** Global distribution of multi-year linear trend at 0.1° for CAMELE, ERA5L,

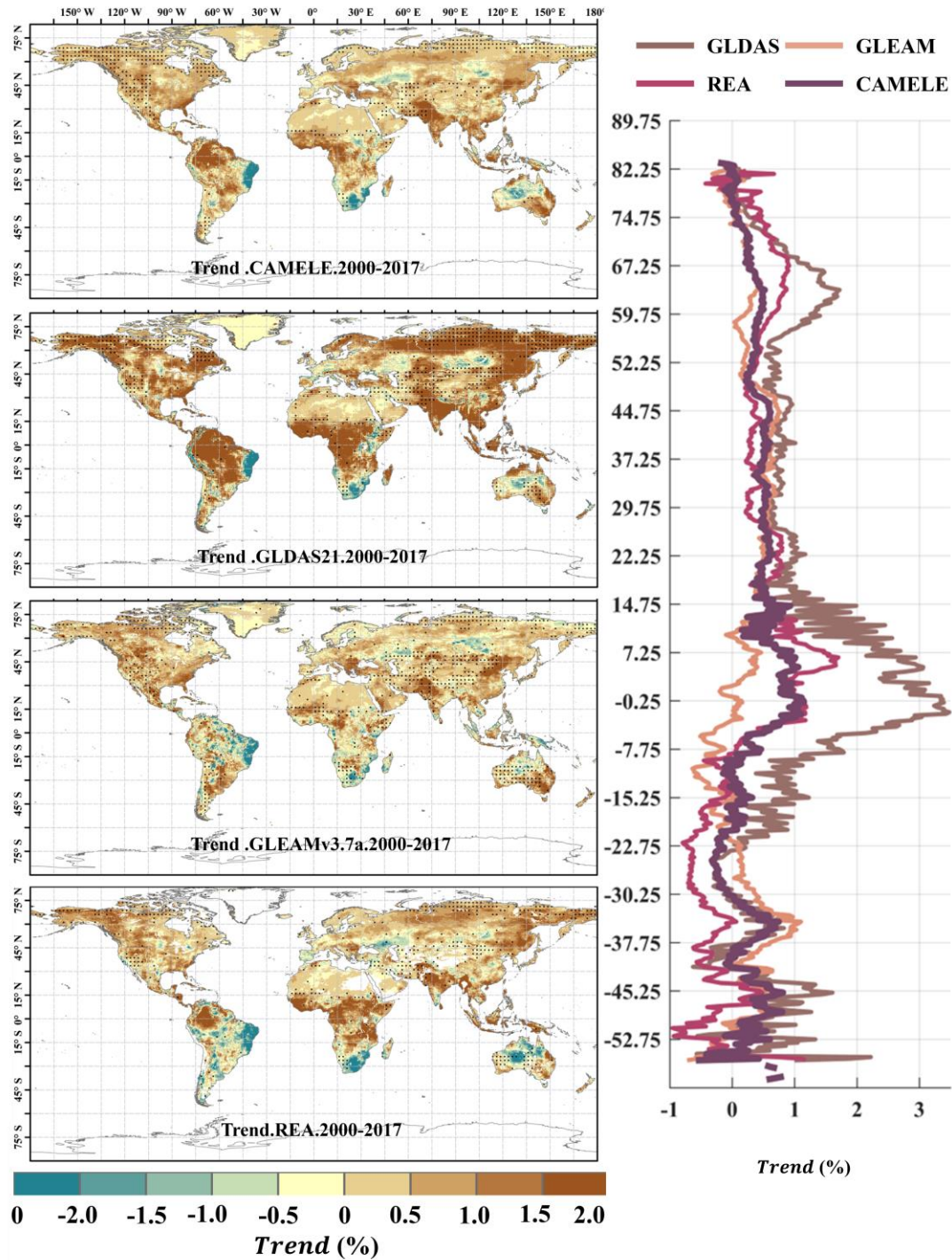
862 FluxCom, and PMLv2, depicted alongside corresponding average trend with latitude.

863 The trend is estimated with Theil–Sen’s slope method, and the significance level is

864 tested with the Mann–Kendall method. The dotted area indicates that the trend has

865 passed the significance test at 5 % level.

866



867

868 **Figure 16** Global distribution of multi-year linear trend at 0.25° for CAMELE,
 869 GLDAS2.1, GLEAMv3.7a, and REA, depicted alongside corresponding average
 870 trend with latitude. The trend is estimated with Theil–Sen’s slope method, and the
 871 significance level is tested with the Mann–Kendall method. The dotted area indicates
 872 that the trend has passed the significance test at 5 % level.

873 **Figure 15** 错误!未找到引用源。 and **Figure 16** 错误!未找到引用源。 present the
874 linear trends of multi-year daily scale evapotranspiration (ET) calculated for different
875 products at resolutions of 0.1° and 0.25° , respectively. The corresponding latitude-
876 dependent variations of the rate of change are shown on the right side. It can be
877 observed that the differences in linear trends among the different products are more
878 significant than the multi-year averages, and in some regions, they even exhibit
879 opposite trends. For example, at 0.1° resolution, PMLv2 shows a global increase of
880 1.0% in ET in most regions, while the results from CAMELE, ERA5L, and PMLv2
881 indicate a milder increase in ET in the Amazon rainforest, southern Africa, and
882 northwestern Australia. At 0.25° resolution, except for GLDAS2.1, which shows an
883 apparent global increase in ET, the results from CAMELE, GLEAMv3.7a, and REA
884 indicate milder variations in global ET.

885 **5. Discussion**

886 **5.1. Impact of underlying assumptions in collocation analysis**

887 The collocation analysis system relies on key assumptions, including linearity (linear
888 regression model), stationarity (unchanged probability distribution over time), error
889 orthogonality (independence between random error and true signal), and zero error
890 cross-correlation (independence between random errors). Potential error
891 autocorrelation is considered with lag-1 [day] series. Various studies have examined
892 the validity and impact of these assumptions. Numerous studies have examined the
893 validity of these assumptions and their impact on the outcomes if violated (Tsamalis,
894 2022; Duan et al., 2021; Gruber et al., 2020).

895 The linearity assumption shapes the error model by including additive and
896 multiplicative biases and zero-mean random error. Although some studies have
897 explored the application of a nonlinear rescaling technique (Yilmaz and Crow, 2013;
898 Zwieback et al., 2016), those efforts are primarily limited to soil moisture signals and

899 often fail to accurately represent the true signal unless all datasets share a similar
900 signal-to-noise ratio (SNR). However, it is worth noting that after rescaling processes,
901 such as cumulative distribution function (CDF) matching or climatology removal, the
902 resulting time series (anomalies) are often considered linearly related to the truth since
903 higher-order error terms are removed. In addition, multiplicative relationships have
904 been more commonly identified in rainfall products (Li et al., 2018). In contrast,
905 collocation analysis within the context of ET products frequently suggests that linear
906 relationships are reasonable (Li et al., 2022; Park et al., 2023). Therefore, the linear
907 error model remains a robust implementation, though it has the potential for
908 improvement through rescaling techniques.

909 Regarding violating the stationarity assumption, the evapotranspiration signal does
910 not strictly adhere to this characteristic. However, by collocating triplets with similar
911 magnitude variations, the influence of this violation is minimized. Nonetheless,
912 disparities in climatology between datasets can still arise for various reasons (Su and
913 Ryu, 2015). Several proposed alternatives aim to address this issue, such as removing
914 the climatology of inputs (Stoffelen, 1998; Yilmaz and Crow, 2014; Draper et al.,
915 2013) and subsequently analyzing the random error variance of the anomalies (Dong
916 et al., 2020b). Nevertheless, obtaining a reliable estimation of climatology proves
917 challenging in practice.

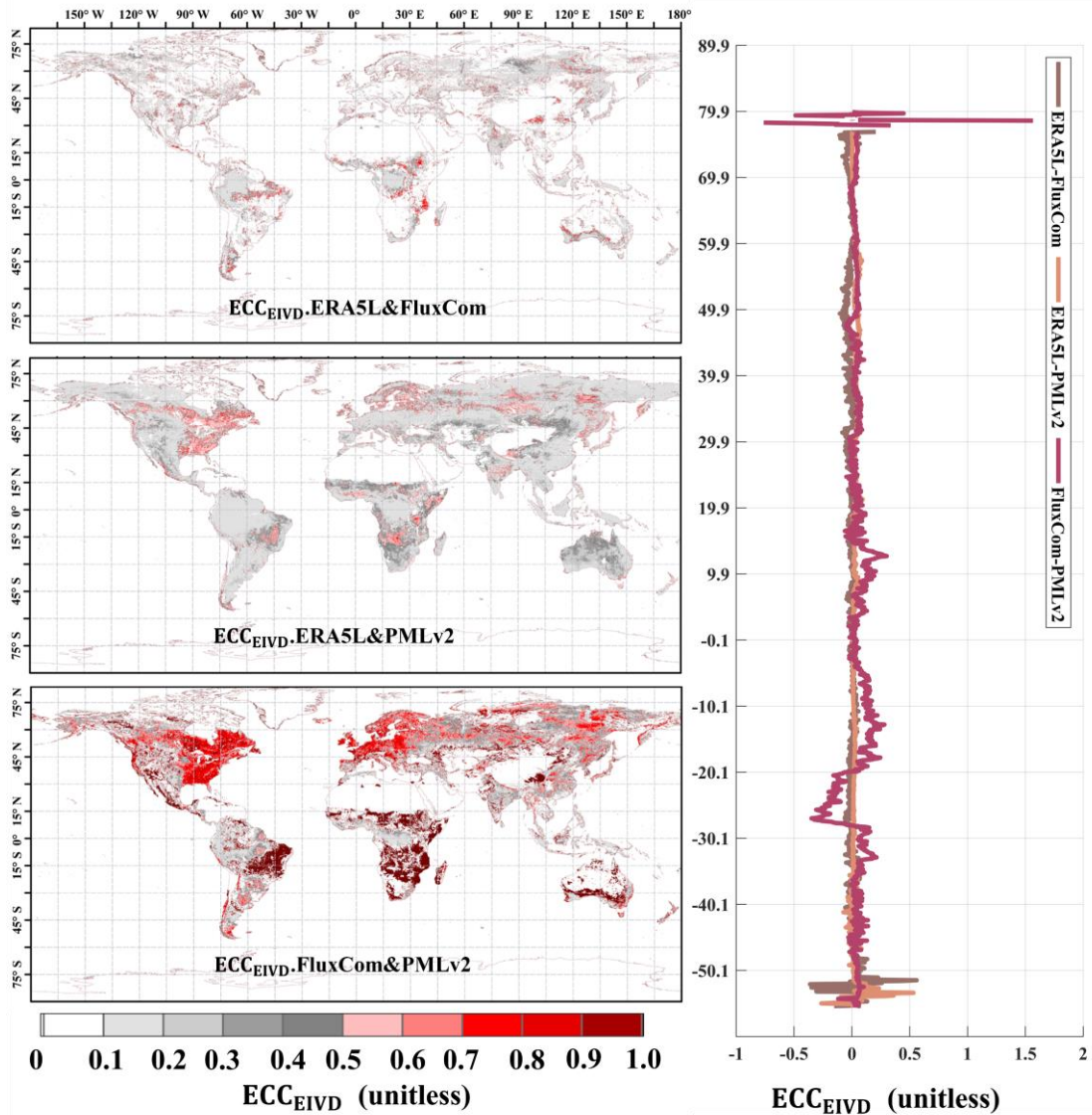
918 The assumption of error orthogonality assumes independence between random error
919 and true signal, i.e., $\sigma_{\varepsilon_t\theta} = 0$. A few studies have examined this assumption. Yilmaz
920 and Crow (2014) investigated such violations using four in situ sites and concluded
921 that the impact is negligible since rescaling mitigates or compensates for bias.
922 Additionally, non-orthogonality results in non-zero error cross-correlation (ECC),
923 although the latter is considered more important. Vogelzang et al. (2022) also
924 investigated this violation recently and demonstrated minimal second-order impact.

925 Non-zero ECC conditions introduce more substantial bias in the results compared to
926 other violations mainly due to two reasons: (1) they cannot be mitigated by rescaling;

927 (2) they cannot be compensated even with equal magnitude for all inputs; and (3) they
928 have been frequently reported in recent studies for various variables (Li et al., 2018,
929 2022; Gruber et al., 2016b). Gruber et al. (2016a) proposed the extended collocation
930 method, which effectively addresses the ECC of selected pairs. Moreover, the EIVD
931 method adopts the error cross-correlation framework. In the following section, we
932 will analyze the ECC between pairs.

933 **5.2. Analysis of error cross-correlation**

934 This study assumes non-zero ECC (Error-Correction Coefficient) conditions exist
935 between FluxCom and PMLv2 at 0.1° and between ERA5L and GLEAM at 0.25° .
936 However, non-zero ECC conditions were also possible between other pairs. Therefore,
937 we presented the EIVD-based ECC results of various pairs.



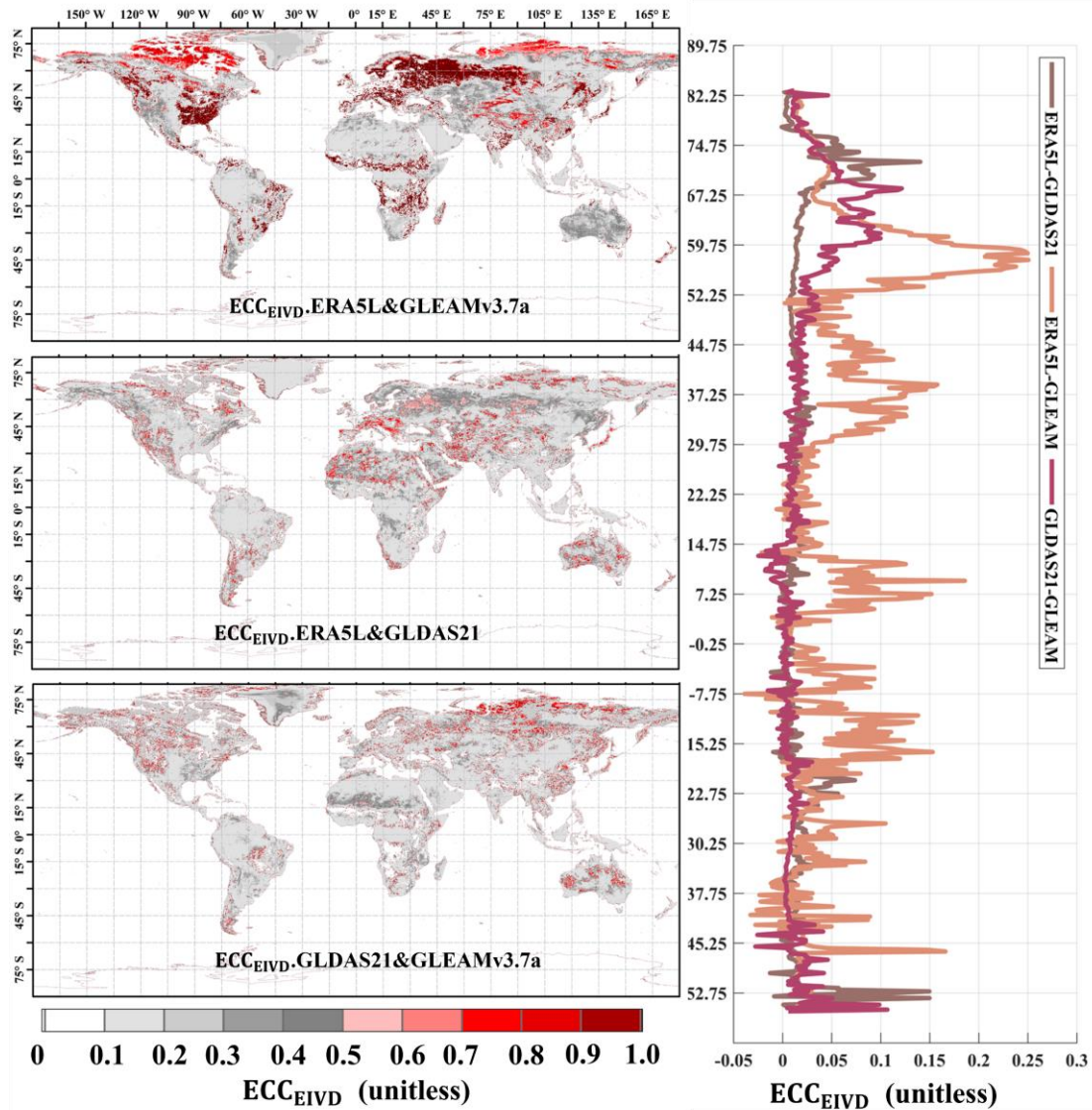
938

939 **Figure 17** Global Distribution of estimated error cross-correlation (ECC) between

940 ERA5L, FluxCom, and PMLv2 pairwise using EIVD alongside relevant variation

941 curves of average with latitude.

942



943

944 **Figure 18** Global Distribution of estimated error cross-correlation (ECC) between

945 ERA5L, GLEAMv3.7a, and GLDAS21 pairwise using EIVD alongside relevant

946 variation curves of average with latitude.

947 As depicted in **Figure 17** and **Figure 18**, at a resolution of 0.1° , the ECC values of

948 FluxCom and PMLv2 were notably higher than those of ERA5L-FluxCom and

949 ERA5L-PMLv2. The global average ECC value for FluxCom-PMLv2 was 0.16, and

950 regions with high ECC values were identified in the eastern United States, most of

951 Europe, and the western Amazon, areas densely covered by measurement sites. Since

952 both FluxCom and PMLv2 incorporated corrections based on FluxNet measurement

953 sites, there is likely some overlap between the sites used by both products in the high

954 ECC regions. This partially explains the shared source of random errors between the
955 two datasets.

956 The global error correlations of GLEAM-GLDAS and ERA5L-GLDAS are relatively
957 low. The random error of ERA5L correlates with that of GLEAM, primarily in arid
958 regions such as the Sahara Desert, Northwest China, and central Australia, where the
959 average ECC exceeds 0.20. The global average ECC of ERA5L-GLEAM is
960 approximately 0.14. A higher error correlation is observed for ERA5L-GLEAM, with
961 a mean ECC value of 0.26, which is expected since meteorological information from
962 ECMWF is reanalyzed for both datasets. However, ECC values for GLEAM-GLDAS
963 and ERA5L-GLDAS are generally low globally, supporting the assumption of zero
964 ECC for these two pairs.

965 Our findings highlight the significant impact of Error Cross Correlation (ECC)
966 between FluxCom-PMLv2 and ERA5L-GLEAM at 0.1° and 0.25° resolutions,
967 respectively. Mathematically, when a triplet exhibits a high ECC value (>0.3)
968 between two sets, it indicates a preference for the remaining independent product as
969 the "better" one, potentially leading to an underestimation of its error variance.
970 However, it is essential to note that the overall ECC values for other pairs are
971 relatively small, suggesting that the zero ECC assumptions can be considered valid
972 for these pairs across most areas. Therefore, these assumptions are unlikely to affect
973 the relevant results of uncertainties significantly. Nevertheless, we have considered
974 the non-zero ECC condition between FluxCom-PMLv2 and ERA5L-GLEAM in this
975 study, as it requires careful consideration.

976 **5.3. Comparison of different fusion schemes**

977 In this section, we conducted comparisons in three aspects: (1) comparing the
978 performance of CAMELE at different resolutions; (2) comparing the performance of
979 different change fusion schemes, explicitly changing the input products' versions
980 (GLDAS21 to GLDAS20 or GLDAS22, GLEAMv3.7a to v3.7b); and (3) comparing

981 the performance of the results obtained without considering the ECC impact.

982 We conducted a comprehensive comparison of our fusion approach with several

983 alternative schemes. Specifically, these schemes encompassed utilizing only ERA5L

984 and PMLV2 at 0.1° based on the IVD method (Comb1), changing the versions of

985 GLDAS2 and GLEAM at 0.25° based on the EIVD method (Comb2-5), and two TC

986 fusion approaches at 0.1° and 0.25°, which did not incorporate ECC.

987 It should be noted that the Comb2 scheme, which includes GLDAS20, covers the

988 period from 1980 to 2014, while the other 0.25° comparison schemes (Comb3-5) span

989 from 2003 to 2022. The combinations based on TC (assuming zero ECC) had the

990 same inputs as CAMELE at both resolutions.

991 **Table 8** Average metrics for CAMELE and other fusion schemes at all sites. The

992 bolded sections indicate the schemes with the best performance in their respective

993 metrics.

Product	RMSE (mm/d)	ubRMSE (mm/d)	MAE (mm/d)	KGE	R
CAMELE (0.1)	0.83	0.71	0.64	0.57	0.71
CAMELE (0.25)	1.03	0.87	0.75	0.51	0.67
ERA5L+PMLV2 (Comb1-0.1 / IVD)	1.13	1.00	0.89	0.46	0.61
ERA5L+GLDAS20+GLEAMv3.7a (Comb2-0.25 / EIVD)	1.09	0.89	0.87	0.44	0.66
ERA5L+GLDAS22+GLEAMv3.7a (Comb3-0.25 / EIVD)	1.20	0.95	0.94	0.44	0.68
ERA5L+GLDAS22+GLEAMv3.7b (Comb4-0.25 / EIVD)	1.19	0.94	0.93	0.44	0.69
ERA5L+GLDAS21+GLEAMv3.7b (Comb5-0.25 / EIVD)	1.05	0.90	0.80	0.49	0.69
ERA5L+FluxCom+PMLv2 (Zero-ECC-0.1 / TC)	1.06	0.91	0.80	0.46	0.60
ERA5L+GLDAS21+GLEAMv3.7a (Zero-ECC-0.25 / TC)	1.26	1.03	0.99	0.39	0.61

994 According to the information in the table, CAMELE (0.1°) results were superior in all

995 indicators. Firstly, when comparing the performance of CAMELE at resolutions of

996 0.1° and 0.25°, it was observed that the fused product performed slightly worse at the

997 0.25° resolution. Additionally, the representative of FluxNet sites at the 0.25°

998 resolution decreased, leading to degraded statistical indicators.

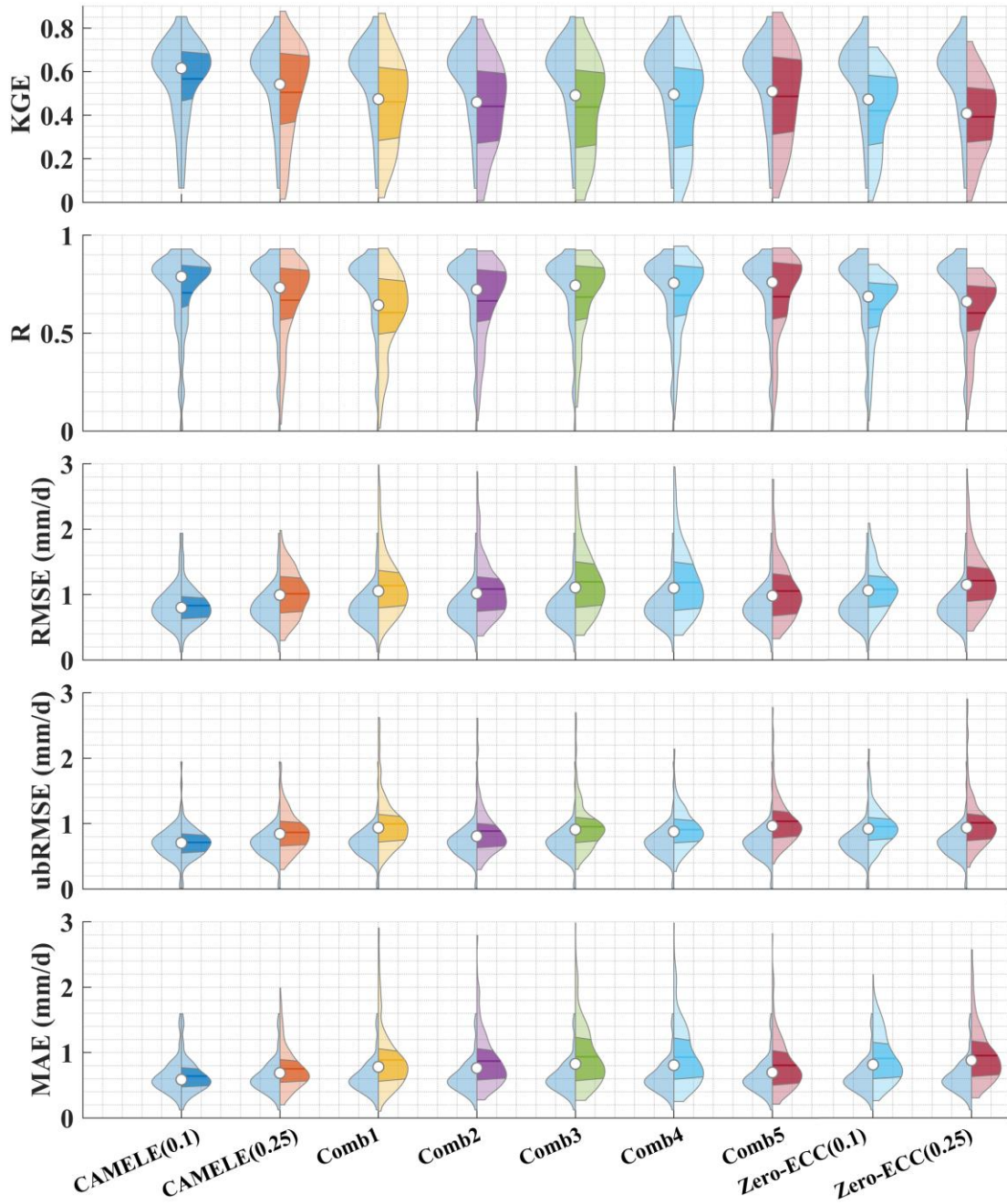
999 At the 0.1° resolution, we conducted a comparison of results obtained by exclusively
1000 fusing ERA5-Land and PMLv2. Multiple indicators indicated that this approach did
1001 not enhance the accuracy of ET estimates and fell significantly short of the scheme
1002 employed in CAMELE. This implies that using only two product sets as input did not
1003 allow for effective error analysis through collocation analysis, resulting in suboptimal
1004 fusion results. More importantly, the limitation of employing only two datasets
1005 prevented us from effectively acquiring error information through collocation analysis
1006 (Dong et al., 2020a, 2019). Consequently, we made the strategic decision to ensure
1007 the inclusion of three datasets as inputs, facilitating the utilization of the EIVD
1008 method and maintaining methodological consistency between the 0.1° and 0.25°
1009 resolutions.

1010 Furthermore, when comparing the results of different fusion schemes between
1011 CAMELE and Comb2-5 at the 0.25° resolution, CAMELE performed better regarding
1012 error metrics (RMSE, ubRMSE, MAE). The differences in fitting metrics (KGE, R)
1013 were insignificant, indicating that the choice of fusion scheme primarily affected the
1014 errors of the fusion results. The relatively poorer performance of other fusion schemes
1015 could be due to the lack of consideration for non-zero ECC. For example, non-zero
1016 ECC between GLDAS-2.2 and ERA5L has been reported in a recent study (Li et al.,
1017 2023a).

1018 For the comparative analysis of the GLDAS2.0 and GLDAS2.1 schemes, the usage of
1019 GLDAS2.1 yielded better performance. The GLDAS-2.1 simulation leverages
1020 conditions from the GLDAS-2.0 simulation, with improved models driven by a
1021 combination of datasets. Previous research has demonstrated that GLDAS-2.1 offers
1022 improvements in the regional-scale simulation of hydrological variables compared to
1023 GLDAS-2.0 (Qi et al., 2018, 2020). Consequently, we chose to incorporate GLDAS-
1024 2.1 data for as much of the time series as possible.

1025 Moreover, when comparing the fusion effects with and without considering non-zero
1026 ECC conditions, it was evident that considering ECC information could effectively

1027 improve the performance of the fused product, which further demonstrated the
 1028 reliability and advantages of the fusion method employed in this study.



1029
 1030 **Figure 19** Violin plot comparing KGE, R, RMSE, ubRMSE and MAE of CAMELE
 1031 with other fusion schemes. The right half of each violin plot represents the
 1032 distribution, with shaded areas indicating the box plot, where the horizontal line
 1033 corresponds to the median and the dot represents the mean. The left half represents
 1034 the results of CAMELE (0.1°) for comparison.

1035 We further provided violin plots for different metrics, comparing the results of each
1036 fusion scheme to CAMELE (0.1°) as shown in **Figure 19**. The results indicated that
1037 the fusion schemes adopted were significantly superior to other schemes based on the
1038 distribution of results for all metrics across all sites. Regarding KGE and R,
1039 CAMELE's results were concentrated near 1 for most sites. Regarding RMSE,
1040 ubRMSE, and MAE, their results were concentrated below one mm/d. The results in
1041 the plots also suggested that CAMELE performed slightly worse at 0.25° compared to
1042 0.1° but still outperformed other combination results. Additionally, comparing
1043 CAMELE and the zero-ECC scheme in the plots further highlighted the importance of
1044 considering non-zero ECC conditions.

1045 **5.4. Potential Applications and Future Enhancements**

1046 In this section, we delve into the potential applications of our product and outline our
1047 commitment to future enhancements to maintain its accuracy and relevance.

1048 Here, we identify three potential applications for our transpiration product: (1) Global
1049 ET Trends: Our product facilitates global-scale analysis of current ET patterns and
1050 long-term trends, essential for comprehending ecosystem responses to evolving
1051 environmental conditions in a warming climate; (2) Transpiration-to-
1052 Evapotranspiration Ratio: Our merging approach can fuse multi-source global gridded
1053 transpiration data, allowing for the examination of the transpiration-to-
1054 evapotranspiration ratio. This analysis can enhance water resource management and
1055 water availability predictions in diverse regions; (3) Attribution analysis: Our product
1056 is a valuable tool for attribution analysis, helping researchers identify the drivers of
1057 patterns. This knowledge is crucial for understanding the roles of climate variability,
1058 land-use changes, and other factors in shaping terrestrial water fluxes.

1059 Furthermore, we are committed to enhancing our product proactively. Key strategies
1060 include: (1) Data Update and Validation: To ensure our product's continued accuracy
1061 and reliability, we will prioritize regularly updating the data used in this study to the

1062 latest versions. By adopting this approach, we aim to provide users with results that
1063 reflect the latest advancements in scientific knowledge; (2) Enhanced Integration and
1064 Error Reduction: We continually refine estimates by incorporating additional data
1065 sources and implementing extended collocation method to minimize errors; (3)
1066 Integration of High-Resolution Regional ET Data: Recognizing the significance of
1067 regional-scale insights, we will focus on improving the accuracy of CAMELE by
1068 integrating higher-resolution regional ET data. This integration will enable more
1069 precise regional estimation.

1070 In summary, these endeavors collectively represent our commitment to maintaining
1071 our product's quality and relevance, ensuring its value for the scientific community.

1072 **6. Conclusion**

1073 This study used a collocation-based approach for merging data considering non-zero
1074 conditions. We successfully generated a long-term daily CAMELE evapotranspiration
1075 (ET) product at resolutions of 0.1° (2000 to 2020) and 0.25° (1980 to 2022) by
1076 integrating five widely used datasets: ERA5L, FluxCom, PMLv2, GLDAS, and
1077 GLEAM. The key findings of our study are as follows:

- 1078 1. Collocation analysis methods proved to be a reliable tool for evaluating ET
1079 products without a reference dataset. This approach shows promising potential for
1080 error characterization, especially in regions with limited data availability or on a
1081 global scale. The evaluation results provided valuable insights into the data
1082 merging process.
- 1083 2. Compared to five input products, REA, and simple average, the CAMELE product
1084 performed well when evaluated against FluxNet flux tower data. While CAMELE
1085 may not excel in all individual metrics, it effectively reduces errors associated
1086 with the input products. The result showed Pearson correlation coefficients (R) of
1087 0.63 and 0.65, root-mean-square errors (RMSE) of 0.81 and 0.73 mm/d, unbiased
1088 root-mean-square errors (ubRMSE) of 1.20 and 1.04 mm/d, mean absolute errors

1089 (MAE) of 0.81 and 0.73 mm/d, and Kling-Gupta efficiency (KGE) of 0.60 and
1090 0.65 on average over resolutions of 0.1° and 0.25°, respectively. This robust
1091 performance is especially evident when assessing its comprehensive station-scale
1092 evaluation.

1093 3. For different plant functional types (PFTs), the CAMELE product outperformed
1094 the five input products, REA, and simple average in most PFTs. Although
1095 FluxCom and PMLv2 performed slightly better than CAMELE at some PFT sites,
1096 considering that both utilized FluxNet sites for product calibration, it indirectly
1097 demonstrates the promising and robust performance of CAMELE.

1098 4. Based on site-scale observations, CAMELE effectively captures the multi-year
1099 linear trend of ET. The accuracy of the multi-year mean value depicted by
1100 CAMELE is improved compared to the input data. Moreover, it accurately
1101 characterizes extreme ET values. However, there is a slight overestimation in
1102 representing the seasonality, which needs further improvement in future research.

1103 5. When utilizing the error information derived from collocation analysis for
1104 merging, it is crucial to consider the potential presence of non-zero error
1105 compensation conditions (ECC). Comparing the merging schemes with and
1106 without considering non-zero ECC, it was found that considering ECC improves
1107 the accuracy of the merging process. Additionally, when using collocation
1108 analysis, it is necessary to identify which products may have ECC in advance,
1109 providing more effective support for data merging and obtaining more accurate
1110 product error information.

1111 In conclusion, our proposed collocation-based data merging approach demonstrates
1112 the promising potential for merging ET products. The resulting CAMELE product
1113 exhibited good overall performance at site-based and regional scales, meeting the
1114 requirements for more detailed research. Furthermore, further evaluation of the
1115 merged product in specific regions is necessary to improve its accuracy. In future
1116 studies, dynamic weights could be computed by considering suitable merging periods

1117 for different products to enhance the quality of the merged product, and more
1118 sophisticated combination schemes could be explored to improve accuracy.

1119 **Author Contribution**

1120 C.L. conceived and designed the study, collected and analyzed the data, and wrote the
1121 manuscript. H.Y participated in the study design, provided intellectual insights, and
1122 reviewed the manuscript for important intellectual content. Z.L. and W.Y provided
1123 substantial input in the study design and data interpretation and revised the manuscript.
1124 Z.T., J.H., and S.L. guided the research process and critically reviewed the manuscript.
1125 All authors have read and approved the final version of the manuscript.

1126 **Competing interests**

1127 The authors declare that they have no conflict of interest.

1128 **Acknowledgments**

1129 This research was supported by the China National Key R&D Program (grant no.
1130 2022YFC3002802), the National Natural Science Foundation of China (grant nos.
1131 51979140, 52309022 and 42041004), and the Key Research and Development
1132 Program of Yunnan Province, China (grant no. 202203AA080010).

1133 **Data and code availability**

1134 The datasets utilized in this research can be accessed through the links provided in the
1135 Dataset Section. The CAMELE products are available via
1136 <https://doi.org/10.5281/zenodo.5704736> (Li et al., 2023b). The data is distributed
1137 under a Creative Commons Attribution 4.0 License. Additionally, we provide
1138 example MATLAB codes to read and plot CAMELE data and employ IVD and EIVD
1139 methods to merge the inputs. Please refer to the latest version., 202306.

1141 **Reference**

- 1142 Baker, J. C. A., Garcia-Carreras, L., Gloor, M., Marsham, J. H., Buermann, W., da
1143 Rocha, H. R., Nobre, A. D., de Araujo, A. C., and Spracklen, D. V.:
1144 Evapotranspiration in the Amazon: spatial patterns, seasonality, and recent trends in
1145 observations, reanalysis, and climate models, *Hydrology and Earth System Sciences*,
1146 25, 2279–2300, <https://doi.org/10.5194/hess-25-2279-2021>, 2021.
- 1147 Barraza Bernadas, V., Grings, F., Restrepo-Coupe, N., and Huete, A.: Comparison of
1148 the performance of latent heat flux products over southern hemisphere forest
1149 ecosystems: estimating latent heat flux error structure using in situ measurements and
1150 the triple collocation method, *International Journal of Remote Sensing*, 39, 6300–
1151 6315, 2018.
- 1152 Bates, J. M. and Granger, C. W.: The combination of forecasts, *Journal of the*
1153 *Operational Research Society*, 20, 451–468, 1969.
- 1154 Chen, Z., Zhu, Z., Jiang, H., and Sun, S.: Estimating daily reference
1155 evapotranspiration based on limited meteorological data using deep learning and
1156 classical machine learning methods, *Journal of Hydrology*, 591,
1157 <https://doi.org/10.1016/j.jhydrol.2020.125286>, 2020.
- 1158 De Lannoy, G. J., Houser, P. R., Verhoest, N. E., Pauwels, V. R., and Gish, T. J.:
1159 Upscaling of point soil moisture measurements to field averages at the OPE3 test site,
1160 *Journal of Hydrology*, 343, 1–11, 2007.
- 1161 Deng, X., Zhu, L., Wang, H., Zhang, X., Tong, C., Li, S., and Wang, K.: Triple
1162 Collocation Analysis and In Situ Validation of the CYGNSS Soil Moisture Product,
1163 *IEEE Journal of Selected Topics in Applied Earth Observations and Remote Sensing*,
1164 16, 1883–1899, <https://doi.org/10.1109/jstars.2023.3235111>, 2023.
- 1165 Dong, J. and Crow, W. T.: An Improved Triple Collocation Analysis Algorithm for
1166 Decomposing Autocorrelated and White Soil Moisture Retrieval Errors, *Journal of*
1167 *Geophysical Research: Atmospheres*, 122, 13,081–13,094,
1168 <https://doi.org/10.1002/2017jd027387>, 2017.
- 1169 Dong, J., Crow, W. T., Duan, Z., Wei, L., and Lu, Y.: A double instrumental variable
1170 method for geophysical product error estimation, *Remote Sensing of Environment*,
1171 225, 217–228, <https://doi.org/10.1016/j.rse.2019.03.003>, 2019.
- 1172 Dong, J., Wei, L., Chen, X., Duan, Z., and Lu, Y.: An instrument variable based
1173 algorithm for estimating cross-correlated hydrological remote sensing errors, *Journal*
1174 *of Hydrology*, 581, 124413, <https://doi.org/10.1016/j.jhydrol.2019.124413>, 2020a.

1175 Dong, J., Lei, F., and Wei, L.: Triple Collocation Based Multi-Source Precipitation
1176 Merging, *Frontiers in Water*, 2, <https://doi.org/10.3389/frwa.2020.00001>, 2020b.

1177 Dong, J., Crow, W. T., Chen, X., Tangdamrongsub, N., Gao, M., Sun, S., Qiu, J., Wei,
1178 L., Gao, H., and Duan, Z.: Statistical uncertainty analysis-based precipitation merging
1179 (SUPER): A new framework for improved global precipitation estimation, *Remote
1180 Sensing of Environment*, 283, 113299, <https://doi.org/10.1016/j.rse.2022.113299>,
1181 2022.

1182 Draper, C., Reichle, R., de Jeu, R., Naeimi, V., Parinussa, R., and Wagner, W.:
1183 Estimating root mean square errors in remotely sensed soil moisture over continental
1184 scale domains, *Remote Sensing of Environment*, 137, 288–298, 2013.

1185 Duan, Z., Duggan, E., Chen, C., Gao, H., Dong, J., and Liu, J.: Comparison of
1186 traditional method and triple collocation analysis for evaluation of multiple gridded
1187 precipitation products across Germany, *Journal of Hydrometeorology*,
1188 <https://doi.org/10.1175/JHM-D-21-0049.1>, 2021.

1189 ECMWF, S. P.: In IFS documentation CY40R1 Part IV: Physical Processes, ECMWF:
1190 Reading, UK, 111–113, 2014.

1191 Ershadi, A., McCabe, M. F., Evans, J. P., Chaney, N. W., and Wood, E. F.: Multi-site
1192 evaluation of terrestrial evaporation models using FLUXNET data, *Agricultural and
1193 Forest Meteorology*, 187, 46–61, <https://doi.org/10.1016/j.agrformet.2013.11.008>,
1194 2014.

1195 Feng, Y., Cui, N., Zhao, L., Hu, X., and Gong, D.: Comparison of ELM, GANN,
1196 WNN and empirical models for estimating reference evapotranspiration in humid
1197 region of Southwest China, *Journal of Hydrology*, 536, 376–383,
1198 <https://doi.org/10.1016/j.jhydrol.2016.02.053>, 2016.

1199 Gan, R., Zhang, Y., Shi, H., Yang, Y., Eamus, D., Cheng, L., Chiew, F. H., and Yu,
1200 Q.: Use of satellite leaf area index estimating evapotranspiration and gross
1201 assimilation for Australian ecosystems, *Ecohydrology*, 11, e1974, 2018.

1202 Gentine, P., Massmann, A., Lintner, B. R., Hamed Alemohammad, S., Fu, R., Green,
1203 J. K., Kennedy, D., and Vilà-Guerau de Arellano, J.: Land–atmosphere interactions in
1204 the tropics – a review, *Hydrology and Earth System Sciences*, 23, 4171–4197,
1205 <https://doi.org/10.5194/hess-23-4171-2019>, 2019.

1206 Gruber, A., Su, C., Crow, W. T., Zwieback, S., Dorigo, W., and Wagner, W.:
1207 Estimating error cross-correlations in soil moisture data sets using extended
1208 collocation analysis, *Journal of Geophysical Research: Atmospheres*, 121, 1208–1219,
1209 2016a.

- 1210 Gruber, A., Su, C.-H., Zwieback, S., Crow, W., Dorigo, W., and Wagner, W.: Recent
1211 advances in (soil moisture) triple collocation analysis, *International Journal of*
1212 *Applied Earth Observation and Geoinformation*, 45, 200–211,
1213 <https://doi.org/10.1016/j.jag.2015.09.002>, 2016b.
- 1214 Gruber, A., Dorigo, W. A., Crow, W., and Wagner, W.: Triple Collocation-Based
1215 Merging of Satellite Soil Moisture Retrievals, *IEEE Trans. Geosci. Remote Sensing*,
1216 55, 6780–6792, <https://doi.org/10.1109/TGRS.2017.2734070>, 2017.
- 1217 Gruber, A., Scanlon, T., van der Schalie, R., Wagner, W., and Dorigo, W.: Evolution
1218 of the ESA CCI Soil Moisture climate data records and their underlying merging
1219 methodology, *Earth System Science Data*, 11, 717–739, [https://doi.org/10.5194/essd-](https://doi.org/10.5194/essd-11-717-2019)
1220 11-717-2019, 2019.
- 1221 Gruber, A., De Lannoy, G., Albergel, C., Al-Yaari, A., Brocca, L., Calvet, J. C.,
1222 Colliander, A., Cosh, M., Crow, W., Dorigo, W., Draper, C., Hirschi, M., Kerr, Y.,
1223 Konings, A., Lahoz, W., McColl, K., Montzka, C., Muñoz-Sabater, J., Peng, J.,
1224 Reichle, R., Richaume, P., Rüdiger, C., Scanlon, T., van der Schalie, R., Wigneron, J.
1225 P., and Wagner, W.: Validation practices for satellite soil moisture retrievals: What
1226 are (the) errors?, *Remote Sensing of Environment*, 244, 111806,
1227 <https://doi.org/10.1016/j.rse.2020.111806>, 2020.
- 1228 Gupta, H. V., Kling, H., Yilmaz, K. K., and Martinez, G. F.: Decomposition of the
1229 mean squared error and NSE performance criteria: Implications for improving
1230 hydrological modelling, *Journal of hydrology*, 377, 80–91, 2009.
- 1231 Han, S. and Tian, F.: A review of the complementary principle of evaporation: from
1232 the original linear relationship to generalized nonlinear functions, *Hydrology and*
1233 *Earth System Sciences*, 24, 2269–2285, <https://doi.org/10.5194/hess-24-2269-2020>,
1234 2020.
- 1235 Hao, Y., Baik, J., and Choi, M.: Combining generalized complementary relationship
1236 models with the Bayesian Model Averaging method to estimate actual
1237 evapotranspiration over China, *Agricultural and Forest Meteorology*, 279, 107759,
1238 <https://doi.org/10.1016/j.agrformet.2019.107759>, 2019.
- 1239 Hersbach, H., Bell, B., Berrisford, P., Hirahara, S., Horányi, A., Muñoz-Sabater, J.,
1240 Nicolas, J., Peubey, C., Radu, R., Schepers, D., Simmons, A., Soci, C., Abdalla, S.,
1241 Abellan, X., Balsamo, G., Bechtold, P., Biavati, G., Bidlot, J., Bonavita, M., Chiara,
1242 G., Dahlgren, P., Dee, D., Diamantakis, M., Dragani, R., Flemming, J., Forbes, R.,
1243 Fuentes, M., Geer, A., Haimberger, L., Healy, S., Hogan, R. J., Hólm, E., Janisková,
1244 M., Keeley, S., Laloyaux, P., Lopez, P., Lupu, C., Radnoti, G., Rosnay, P., Rozum, I.,
1245 Vamborg, F., Villaume, S., and Thépaut, J.: The ERA5 global reanalysis, *Quarterly*
1246 *Journal of the Royal Meteorological Society*, 146, 1999–2049,

- 1247 <https://doi.org/10.1002/qj.3803>, 2020.
- 1248 Hoareau, N., Portabella, M., Lin, W., Ballabrera-Poy, J., and Turiel, A.: Error
1249 characterization of sea surface salinity products using triple collocation analysis,
1250 *IEEE Transactions on Geoscience and Remote Sensing*, 56, 5160–5168, 2018.
- 1251 Jia, Y., Li, C., Yang, H., Yang, W., and Liu, Z.: Assessments of three
1252 evapotranspiration products over China using extended triple collocation and water
1253 balance methods, *Journal of Hydrology*, 614, 128594, 2022.
- 1254 Jiang, C. and Ryu, Y.: Multi-scale evaluation of global gross primary productivity and
1255 evapotranspiration products derived from Breathing Earth System Simulator (BESS),
1256 *Remote Sensing of Environment*, 186, 528–547, 2016.
- 1257 Jiang, C., Ryu, Y., Fang, H., Myneni, R., Claverie, M., and Zhu, Z.: Inconsistencies of
1258 interannual variability and trends in long-term satellite leaf area index products, *Glob
1259 Chang Biol*, 23, 4133–4146, <https://doi.org/10.1111/gcb.13787>, 2017.
- 1260 Jiang, C., Guan, K., Pan, M., Ryu, Y., Peng, B., and Wang, S.: BESS-STAIR: a
1261 framework to estimate daily, 30 m, and all-weather crop evapotranspiration using
1262 multi-source satellite data for the US Corn Belt, *Hydrology and Earth System
1263 Sciences*, 24, 1251–1273, <https://doi.org/10.5194/hess-24-1251-2020>, 2020.
- 1264 Jiménez, C., Prigent, C., Mueller, B., Seneviratne, S. I., McCabe, M. F., Wood, E. F.,
1265 Rossow, W. B., Balsamo, G., Betts, A. K., Dirmeyer, P. A., Fisher, J. B., Jung, M.,
1266 Kanamitsu, M., Reichle, R. H., Reichstein, M., Rodell, M., Sheffield, J., Tu, K., and
1267 Wang, K.: Global intercomparison of 12 land surface heat flux estimates, *Journal of
1268 Geophysical Research*, 116, <https://doi.org/10.1029/2010jd014545>, 2011.
- 1269 Jung, M., Koirala, S., Weber, U., Ichii, K., Gans, F., Camps-Valls, G., Papale, D.,
1270 Schwalm, C., Tramontana, G., and Reichstein, M.: The FLUXCOM ensemble of
1271 global land-atmosphere energy fluxes, *Sci Data*, 6, 74,
1272 <https://doi.org/10.1038/s41597-019-0076-8>, 2019.
- 1273 Khan, M. S., Liaqat, U. W., Baik, J., and Choi, M.: Stand-alone uncertainty
1274 characterization of GLEAM, GLDAS and MOD16 evapotranspiration products using
1275 an extended triple collocation approach, *Agricultural and Forest Meteorology*, 252,
1276 256–268, <https://doi.org/10.1016/j.agrformet.2018.01.022>, 2018.
- 1277 Kim, S., Pham, H. T., Liu, Y. Y., Marshall, L., and Sharma, A.: Improving the
1278 Combination of Satellite Soil Moisture Data Sets by Considering Error Cross
1279 Correlation: A Comparison Between Triple Collocation (TC) and Extended Double
1280 Instrumental Variable (EIVD) Alternatives, *IEEE Transactions on Geoscience and
1281 Remote Sensing*, 59, 7285–7295, <https://doi.org/10.1109/tgrs.2020.3032418>, 2021a.

- 1282 Kim, S., Sharma, A., Liu, Y. Y., and Young, S. I.: Rethinking satellite data merging:
1283 from averaging to SNR optimization, *IEEE Transactions on Geoscience and Remote*
1284 *Sensing*, 60, 1–15, 2021b.
- 1285 Kling, H., Fuchs, M., and Paulin, M.: Runoff conditions in the upper Danube basin
1286 under an ensemble of climate change scenarios, *Journal of Hydrology*, 424–425, 264–
1287 277, <https://doi.org/10.1016/j.jhydrol.2012.01.011>, 2012.
- 1288 Knoben, W. J. M., Freer, J. E., and Woods, R. A.: Technical note: Inherent
1289 benchmark or not? Comparing Nash–Sutcliffe and Kling–Gupta efficiency scores,
1290 *Hydrology and Earth System Sciences*, 23, 4323–4331, [https://doi.org/10.5194/hess-](https://doi.org/10.5194/hess-23-4323-2019)
1291 [23-4323-2019](https://doi.org/10.5194/hess-23-4323-2019), 2019.
- 1292 Koster, R. D., Liu, Q., Reichle, R. H., and Huffman, G. J.: Improved Estimates of
1293 Pentad Precipitation Through the Merging of Independent Precipitation Data Sets,
1294 *Water Resources Research*, 57, <https://doi.org/10.1029/2021wr030330>, 2021.
- 1295 Leuning, R., Zhang, Y., Rajaud, A., Cleugh, H., and Tu, K.: A simple surface
1296 conductance model to estimate regional evaporation using MODIS leaf area index and
1297 the Penman-Monteith equation, *Water Resources Research*, 44, 2008.
- 1298 Leuning, R., Zhang, Y. Q., Rajaud, A., Cleugh, H., and Tu, K.: Correction to “A
1299 simple surface conductance model to estimate regional evaporation using MODIS leaf
1300 area index and the Penman-Monteith equation,” *Water Resources Research*, 45,
1301 <https://doi.org/10.1029/2008wr007631>, 2009.
- 1302 Li, B., Rodell, M., Kumar, S., Beaudoin, H. K., Getirana, A., Zaitchik, B. F.,
1303 Goncalves, L. G., Cossetin, C., Bhanja, S., Mukherjee, A., Tian, S., Tangdamrongsub,
1304 N., Long, D., Nanteza, J., Lee, J., Policelli, F., Goni, I. B., Daira, D., Bila, M., Lannoy,
1305 G., Mocko, D., Steele-Dunne, S. C., Save, H., and Bettadpur, S.: Global GRACE Data
1306 Assimilation for Groundwater and Drought Monitoring: Advances and Challenges,
1307 *Water Resour. Res.*, 55, 7564–7586, <https://doi.org/10.1029/2018WR024618>, 2019a.
- 1308 Li, C., Tang, G., and Hong, Y.: Cross-evaluation of ground-based, multi-satellite and
1309 reanalysis precipitation products: Applicability of the Triple Collocation method
1310 across Mainland China, *Journal of Hydrology*, 562, 71–83,
1311 <https://doi.org/10.1016/j.jhydrol.2018.04.039>, 2018.
- 1312 Li, C., Yang, H., Yang, W., Liu, Z., Jia, Y., Li, S., and Yang, D.: Error
1313 Characterization of Global Land Evapotranspiration Products: Collocation-based
1314 approach, *Journal of Hydrology*, 128102, 2022.
- 1315 Li, C., Liu, Z., Tu, Z., Shen, J., He, Y., and Yang, H.: Assessment of global gridded
1316 transpiration products using the extended instrumental variable technique (EIVD),
1317 *Journal of Hydrology*, 623, 129880, <https://doi.org/10.1016/j.jhydrol.2023.129880>,

- 1318 2023a.
- 1319 Li, C., Liu, Z., Yang, W., Tu, Z., Han, J., Sien, L., and Hanbo, Y.: CAMELE:
1320 Collocation-Analyzed Multi-source Ensembled Land Evapotranspiration Data, ,
1321 <https://doi.org/10.5281/zenodo.8047038>, 2023b.
- 1322 Li, X., Gentine, P., Lin, C., Zhou, S., Sun, Z., Zheng, Y., Liu, J., and Zheng, C.: A
1323 simple and objective method to partition evapotranspiration into transpiration and
1324 evaporation at eddy-covariance sites, *Agricultural and Forest Meteorology*, 265, 171–
1325 182, <https://doi.org/10.1016/j.agrformet.2018.11.017>, 2019b.
- 1326 Li, X., Zhang, W., Vermeulen, A., Dong, J., and Duan, Z.: Triple collocation-based
1327 merging of multi-source gridded evapotranspiration data in the Nordic Region,
1328 *Agricultural and Forest Meteorology*, 335, 109451,
1329 <https://doi.org/10.1016/j.agrformet.2023.109451>, 2023c.
- 1330 Lian, X., Piao, S., Huntingford, C., Li, Y., Zeng, Z., Wang, X., Ciais, P., McVicar, T.
1331 R., Peng, S., Ottlé, C., Yang, H., Yang, Y., Zhang, Y., and Wang, T.: Partitioning
1332 global land evapotranspiration using CMIP5 models constrained by observations,
1333 *Nature Clim Change*, 8, 640–646, <https://doi.org/10.1038/s41558-018-0207-9>, 2018.
- 1334 Lin, C., Gentine, P., Huang, Y., Guan, K., Kimm, H., and Zhou, S.: Diel ecosystem
1335 conductance response to vapor pressure deficit is suboptimal and independent of soil
1336 moisture, *Agricultural and Forest Meteorology*, 250, 24–34, 2018.
- 1337 Loveland, T. R., Zhu, Z., Ohlen, D. O., Brown, J. F., Reed, B. C., and Yang, L.: An
1338 analysis of the IGBP global land-cover characterization process, *Photogrammetric
1339 engineering and remote sensing*, 65, 1021–1032, 1999.
- 1340 Lu, J., Wang, G., Chen, T., Li, S., Hagan, D. F. T., Kattel, G., Peng, J., Jiang, T., and
1341 Su, B.: A harmonized global land evaporation dataset from model-based products
1342 covering 1980–2017, *Earth System Science Data*, 13, 5879–5898,
1343 <https://doi.org/10.5194/essd-13-5879-2021>, 2021.
- 1344 Ma, N., Szilagyi, J., and Jozsa, J.: Benchmarking large-scale evapotranspiration
1345 estimates: A perspective from a calibration-free complementary relationship approach
1346 and FLUXCOM, *Journal of Hydrology*, 590,
1347 <https://doi.org/10.1016/j.jhydrol.2020.125221>, 2020.
- 1348 Majozi, N. P., Mannaerts, C. M., Ramoelo, A., Mathieu, R., Nickless, A., and Verhoef,
1349 W.: Analysing surface energy balance closure and partitioning over a semi-arid
1350 savanna FLUXNET site in Skukuza, Kruger National Park, South Africa, *Hydrology
1351 and Earth System Sciences*, 21, 3401–3415, [https://doi.org/10.5194/hess-21-3401-
1352 2017](https://doi.org/10.5194/hess-21-3401-2017), 2017.

- 1353 Martens, B., Miralles, D. G., Lievens, H., van der Schalie, R., de Jeu, R. A. M.,
1354 Fernández-Prieto, D., Beck, H. E., Dorigo, W. A., and Verhoest, N. E. C.:
1355 GLEAM v3: satellite-based land evaporation and root-zone soil moisture,
1356 Geoscientific Model Development, 10, 1903–1925, [https://doi.org/10.5194/gmd-10-](https://doi.org/10.5194/gmd-10-1903-2017)
1357 1903-2017, 2017.
- 1358 McColl, K. A., Vogelzang, J., Konings, A. G., Entekhabi, D., Piles, M., and Stoffelen,
1359 A.: Extended triple collocation: Estimating errors and correlation coefficients with
1360 respect to an unknown target, Geophysical Research Letters, 41, 6229–6236,
1361 <https://doi.org/10.1002/2014gl061322>, 2014.
- 1362 Ming, W., Ji, X., Zhang, M., Li, Y., Liu, C., Wang, Y., and Li, J.: A Hybrid Triple
1363 Collocation-Deep Learning Approach for Improving Soil Moisture Estimation from
1364 Satellite and Model-Based Data, Remote Sensing, 14,
1365 <https://doi.org/10.3390/rs14071744>, 2022.
- 1366 Miralles, D., De Jeu, R., Gash, J., Holmes, T., and Dolman, A.: Magnitude and
1367 variability of land evaporation and its components at the global scale, Hydrology and
1368 Earth System Sciences, 15, 967–981, 2011.
- 1369 Miralles, D. G., Gentine, P., Seneviratne, S. I., and Teuling, A. J.: Land-atmospheric
1370 feedbacks during droughts and heatwaves: state of the science and current challenges,
1371 Ann N Y Acad Sci, 1436, 19–35, <https://doi.org/10.1111/nyas.13912>, 2019.
- 1372 Mu, Q., Zhao, M., and Running, S. W.: Improvements to a MODIS global terrestrial
1373 evapotranspiration algorithm, Remote sensing of environment, 115, 1781–1800, 2011.
- 1374 Muñoz-Sabater, J., Dutra, E., Agustí-Panareda, A., Albergel, C., Arduini, G., Balsamo,
1375 G., Boussetta, S., Choulga, M., Harrigan, S., Hersbach, H., Martens, B., Miralles, D.
1376 G., Piles, M., Rodríguez-Fernández, N. J., Zsoter, E., Buontempo, C., and Thépaut, J.-
1377 N.: ERA5-Land: a state-of-the-art global reanalysis dataset for land applications,
1378 Earth Syst. Sci. Data, 13, 4349–4383, <https://doi.org/10.5194/essd-13-4349-2021>,
1379 2021.
- 1380 Pan, S., Pan, N., Tian, H., Friedlingstein, P., Sitch, S., Shi, H., Arora, V. K., Haverd,
1381 V., Jain, A. K., Kato, E., Lienert, S., Lombardozzi, D., Nabel, J. E. M. S., Ottlé, C.,
1382 Poulter, B., Zaehle, S., and Running, S. W.: Evaluation of global terrestrial
1383 evapotranspiration using state-of-the-art approaches in remote sensing, machine
1384 learning and land surface modeling, Hydrology and Earth System Sciences, 24, 1485–
1385 1509, <https://doi.org/10.5194/hess-24-1485-2020>, 2020.
- 1386 Park, J., Baik, J., and Choi, M.: Triple collocation-based multi-source evaporation and
1387 transpiration merging, Agricultural and Forest Meteorology, 331, 109353, 2023.
- 1388 Pastorello, G., Trotta, C., Canfora, E., Chu, H., Christianson, D., Cheah, Y. W.,

1389 Poindexter, C., Chen, J., Elbashandy, A., Humphrey, M., Isaac, P., Polidori, D.,
1390 Reichstein, M., Ribeca, A., van Ingen, C., Vuichard, N., Zhang, L., Amiro, B.,
1391 Ammann, C., Arain, M. A., Ardo, J., Arkebauer, T., Arndt, S. K., Arriga, N., Aubinet,
1392 M., Aurela, M., Baldocchi, D., Barr, A., Beamesderfer, E., Marchesini, L. B.,
1393 Bergeron, O., Beringer, J., Bernhofer, C., Berveiller, D., Billesbach, D., Black, T. A.,
1394 Blanken, P. D., Bohrer, G., Boike, J., Bolstad, P. V., Bonal, D., Bonnefond, J. M.,
1395 Bowling, D. R., Bracho, R., Brodeur, J., Brummer, C., Buchmann, N., Burban, B.,
1396 Burns, S. P., Buysse, P., Cale, P., Cavagna, M., Cellier, P., Chen, S., Chini, I.,
1397 Christensen, T. R., Cleverly, J., Collalti, A., Consalvo, C., Cook, B. D., Cook, D.,
1398 Coursolle, C., Cremonese, E., Curtis, P. S., D'Andrea, E., da Rocha, H., Dai, X.,
1399 Davis, K. J., Cinti, B., Grandcourt, A., Ligne, A., De Oliveira, R. C., Delpierre, N.,
1400 Desai, A. R., Di Bella, C. M., Tommasi, P. D., Dolman, H., Domingo, F., Dong, G.,
1401 Dore, S., Duce, P., Dufrene, E., Dunn, A., Dusek, J., Eamus, D., Eichelmann, U.,
1402 ElKhidir, H. A. M., Eugster, W., Ewenz, C. M., Ewers, B., Famulari, D., Fares, S.,
1403 Feigenwinter, I., Feitz, A., Fensholt, R., Filippa, G., Fischer, M., Frank, J., Galvagno,
1404 M., et al.: The FLUXNET2015 dataset and the ONEFlux processing pipeline for eddy
1405 covariance data, *Sci Data*, 7, 225, <https://doi.org/10.1038/s41597-020-0534-3>, 2020.

1406 Priestley, C. H. B. and TAYLOR, R. J.: On the assessment of surface heat flux and
1407 evaporation using large-scale parameters, *Monthly weather review*, 100, 81–92, 1972.

1408 Qi, W., Liu, J., and Chen, D.: Evaluations and Improvements of GLDAS2.0 and
1409 GLDAS2.1 Forcing Data's Applicability for Basin Scale Hydrological Simulations in
1410 the Tibetan Plateau, *JGR Atmospheres*, 123, <https://doi.org/10.1029/2018JD029116>,
1411 2018.

1412 Qi, W., Liu, J., Yang, H., Zhu, X., Tian, Y., Jiang, X., Huang, X., and Feng, L.: Large
1413 Uncertainties in Runoff Estimations of GLDAS Versions 2.0 and 2.1 in China, *Earth
1414 and Space Science*, 7, e2019EA000829, <https://doi.org/10.1029/2019EA000829>, 2020.

1415 Restrepo-Coupe, N., Albert, L. P., Longo, M., Baker, I., Levine, N. M., Mercado, L.
1416 M., da Araujo, A. C., Christoffersen, B. O., Costa, M. H., Fitzjarrald, D. R., Galbraith,
1417 D., Imbuzeiro, H., Malhi, Y., von Randow, C., Zeng, X., Moorcroft, P., and Saleska,
1418 S. R.: Understanding water and energy fluxes in the Amazonia: Lessons from an
1419 observation-model intercomparison, *Glob Chang Biol*, 27, 1802–1819,
1420 <https://doi.org/10.1111/gcb.15555>, 2021.

1421 Ribal, A. and Young, I. R.: Global Calibration and Error Estimation of Altimeter,
1422 Scatterometer, and Radiometer Wind Speed Using Triple Collocation, *Remote
1423 Sensing*, 12, <https://doi.org/10.3390/rs12121997>, 2020.

1424 Rodell, M., Houser, P., Jambor, U., Gottschalk, J., Mitchell, K., Meng, C.-J.,
1425 Arsenault, K., Cosgrove, B., Radakovich, J., and Bosilovich, M.: The global land data
1426 assimilation system, *Bulletin of the American Meteorological society*, 85, 381–394,

- 1427 2004.
- 1428 Sheffield, J., Goteti, G., and Wood, E. F.: Development of a 50-Year High-Resolution
1429 Global Dataset of Meteorological Forcings for Land Surface Modeling, *Journal of*
1430 *Climate*, 19, 3088–3111, <https://doi.org/10.1175/JCLI3790.1>, 2006.
- 1431 Stoffelen, A.: Toward the true near-surface wind speed: Error modeling and
1432 calibration using triple collocation, *Journal of Geophysical Research: Oceans*, 103,
1433 7755–7766, <https://doi.org/10.1029/97jc03180>, 1998.
- 1434 Su, C.-H. and Ryu, D.: Multi-scale analysis of bias correction of soil moisture,
1435 *Hydrology and Earth System Sciences*, 19, 17–31, 2015.
- 1436 Su, C.-H., Ryu, D., Crow, W. T., and Western, A. W.: Beyond triple collocation:
1437 Applications to soil moisture monitoring, *Journal of Geophysical Research:*
1438 *Atmospheres*, 119, 6419–6439, <https://doi.org/10.1002/2013jd021043>, 2014.
- 1439 Sun, J., McColl, K. A., Wang, Y., Rigden, A. J., Lu, H., Yang, K., Li, Y., and
1440 Santanello, J. A.: Global evaluation of terrestrial near-surface air temperature and
1441 specific humidity retrievals from the Atmospheric Infrared Sounder (AIRS), *Remote*
1442 *Sensing of Environment*, 252, <https://doi.org/10.1016/j.rse.2020.112146>, 2021.
- 1443 Towner, J., Cloke, H. L., Zsoter, E., Flamig, Z., Hoch, J. M., Bazo, J., Coughlan de
1444 Perez, E., and Stephens, E. M.: Assessing the performance of global hydrological
1445 models for capturing peak river flows in the Amazon basin, *Hydrology and Earth*
1446 *System Sciences*, 23, 3057–3080, <https://doi.org/10.5194/hess-23-3057-2019>, 2019.
- 1447 Tsamalis, C.: Clarifications on the equations and the sample number in triple
1448 collocation analysis using SST observations, *Remote Sensing of Environment*, 272,
1449 <https://doi.org/10.1016/j.rse.2022.112936>, 2022.
- 1450 Twine, T. E., Kustas, W., Norman, J., Cook, D., Houser, Pr., Meyers, T., Prueger, J.,
1451 Starks, P., and Wesely, M.: Correcting eddy-covariance flux underestimates over a
1452 grassland, *Agricultural and forest meteorology*, 103, 279–300, 2000.
- 1453 Vogelzang, J., Stoffelen, A., and Verhoef, A.: The Effect of Error Non-Orthogonality
1454 on Triple Collocation Analyses, *Remote Sensing*, 14, 4268, 2022.
- 1455 Wu, K., Ryu, D., Nie, L., and Shu, H.: Time-variant error characterization of SMAP
1456 and ASCAT soil moisture using Triple Collocation Analysis, *Remote Sensing of*
1457 *Environment*, 256, <https://doi.org/10.1016/j.rse.2021.112324>, 2021.
- 1458 Yang, Y., Roderick, M. L., Guo, H., Miralles, D. G., Zhang, L., Fatichi, S., Luo, X.,
1459 Zhang, Y., McVicar, T. R., Tu, Z., Keenan, T. F., Fisher, J. B., Gan, R., Zhang, X.,
1460 Piao, S., Zhang, B., and Yang, D.: Evapotranspiration on a greening Earth, *Nat Rev*

- 1461 Earth Environ, <https://doi.org/10.1038/s43017-023-00464-3>, 2023.
- 1462 Yilmaz, M. T. and Crow, W. T.: The optimality of potential rescaling approaches in
1463 land data assimilation, *Journal of Hydrometeorology*, 14, 650–660, 2013.
- 1464 Yilmaz, M. T. and Crow, W. T.: Evaluation of Assumptions in Soil Moisture Triple
1465 Collocation Analysis, *Journal of Hydrometeorology*, 15, 1293–1302,
1466 <https://doi.org/10.1175/JHM-D-13-0158.1>, 2014.
- 1467 Yilmaz, M. T., Crow, W. T., Anderson, M. C., and Hain, C.: An objective
1468 methodology for merging satellite- and model-based soil moisture products, *Water
1469 Resources Research*, 48, n/a-n/a, <https://doi.org/10.1029/2011wr011682>, 2012.
- 1470 Yin, G. and Park, J.: The use of triple collocation approach to merge satellite- and
1471 model-based terrestrial water storage for flood potential analysis, *Journal of
1472 Hydrology*, 603, <https://doi.org/10.1016/j.jhydrol.2021.127197>, 2021.
- 1473 Yin, L., Tao, F., Chen, Y., Liu, F., and Hu, J.: Improving terrestrial evapotranspiration
1474 estimation across China during 2000–2018 with machine learning methods, *Journal of
1475 Hydrology*, 600, <https://doi.org/10.1016/j.jhydrol.2021.126538>, 2021.
- 1476 Zhang, Y., Leuning, R., Hutley, L. B., Beringer, J., McHugh, I., and Walker, J. P.:
1477 Using long-term water balances to parameterize surface conductances and calculate
1478 evaporation at 0.05 spatial resolution, *Water Resources Research*, 46, 2010.
- 1479 Zhang, Y., Kong, D., Gan, R., Chiew, F. H. S., McVicar, T. R., Zhang, Q., and Yang,
1480 Y.: Coupled estimation of 500 m and 8-day resolution global evapotranspiration and
1481 gross primary production in 2002–2017, *Remote Sensing of Environment*, 222, 165–
1482 182, <https://doi.org/10.1016/j.rse.2018.12.031>, 2019.
- 1483 Zhao, M., Liu, Y., and Konings, A. G.: Evapotranspiration frequently increases during
1484 droughts, *Nature Climate Change*, 1–7, 2022.
- 1485 Zhu, G., Li, X., Zhang, K., Ding, Z., Han, T., Ma, J., Huang, C., He, J., and Ma, T.:
1486 Multi-model ensemble prediction of terrestrial evapotranspiration across north China
1487 using Bayesian model averaging, *Hydrological Processes*, 30, 2861–2879,
1488 <https://doi.org/10.1002/hyp.10832>, 2016.
- 1489 Zwieback, S., Su, C.-H., Gruber, A., Dorigo, W. A., and Wagner, W.: The impact of
1490 quadratic nonlinear relations between soil moisture products on uncertainty estimates
1491 from triple collocation analysis and two quadratic extensions, *Journal of
1492 Hydrometeorology*, 17, 1725–1743, 2016.
- 1493